New Post-Linac Collimation System for the Next Linear Collider

NLC Post-Linac Collimation Task Force
LCC-Note-0052
21-Feb-2001

Abstract

We present a new design for the NLC post-linac collimation system. The new design separates the collimation of off-energy particles and particles with large betatron amplitudes. The energy collimation system achieves passive protection against damage by an errant bunch train via large horizontal dispersion and vertical betatron functions, and makes use of optical symmetries to reduce jitter amplification. The betatron collimation system permits infrequent damage to the thin "spoiler" collimators, while the thick "absorber" collimators have a much larger aperture and are thus more difficult to hit. The physical phenomena which are relevant to the design and operation of the collimation system are reviewed, and the associated properties of the new system are discussed.

Contents

1 Introduction

The principal purpose of the post-linac collimation system is to eliminate any particles which could cause unacceptable background conditions for the detector. The importance of the post-linac collimation system was amply demonstrated by the SLC/SLD experience, in which the backgrounds from the beam "halo" were a serious limitation to performance in the later runs: in order to prevent unacceptable backgrounds it was necessary to reduce the IP divergences below their optima, and reductions in the population and/or the belligerence of the halo were always accompanied by increases in the luminosity [1]. The performance of the FFTB was also impacted by the beam halo, especially during measurements using the Laser Interferometer Beam Size Monitor [2].

The NLC linacs are expected to be similar to the SLC linac in that a new bunch train is accelerated on every machine cycle, and thus the halo is freshly repopulated at the machine rate (unlike storage rings, in which the halo is damped and/or collimated at injection and then is repopulated only slowly during the store). The NLC collimation system faces a more severe task than the SLC's did because of the high beam power, small emittances, and high beam energy. The post-linac collimation system must do the following:

- Remove any particles from the primary beam which would cause unacceptable backgrounds for the detector

- Limit the number of muons, produced at primary beam collimators, which reach the detector and generate backgrounds
- Limit the regeneration of halo due to optical or wakefield phenomena in the collimation system
- Protect the final focus and the detector from a beam with a large betatron amplitude or energy error
- Protect the collimators from being destroyed in the process of protecting the final focus and detector from errant beams
- Limit the deleterious effects of collimator wakefields on the primary beam.

A complete collimation system design for the NLC was presented in 1996 [3]. The optical parameters of the system are shown in Figure 1. The system collimates in both planes (x and y), in both phases ("IP" and "FD" phases, corresponding to particles with large offsets at the interaction point and the final doublet of the final focus, respectively), two iterations per phase/plane combination; energy collimation was also performed in this system. The optical functions of the system were primarily driven by the requirement that one bunch train at full energy (500 GeV per beam) and full charge (10^{12} particles) should be incapable of damaging the collimators in the event of loss of control of the beam. In practical terms this meant that the main collimators (so-called "absorbers," 20 radiation lengths of material) were protected by thin collimators ("spoilers," 0.25 radiation lengths of material) set some distance upstream of them; the spoilers in turn were protected by making the primary beam large at the z location of the spoilers, while generating a large beam divergence via multiple coulomb scattering (MCS) which made the beam even larger at the absorber. The combined requirements of large betatron and dispersion functions and large separations between the spoilers and absorbers resulted in the optics in Figure 1.

The system described in [3] suffered from several shortcomings, all of which were unintended consequences of the passive survival scheme adopted therein. Specifically:

- The system length was approximately 2.5 km per side (5.0 km total)
- The large betatron functions mandated several families of sextupoles for chromatic correction
- The many interleaved sextupole families at all phases made the bandwidth of the collimation system small and the tolerances tight, particularly the tolerances on sextupole alignment
- The large beta functions at both phases implies large $R_{12,34}$ elements from one sector of the collimation system to the next, which in turn meant that quad motions of a few μm in one sector would drive the beam into the collimators in the next sector; only the first two sectors contained spoilers, so the downstream absorbers were at risk from quads drifting diurnally
- The horizontal betatron collimation was interleaved with energy collimation (ie, the x collimators were also collimating in δ); as a result the system required more collimators than it would have needed for separated collimation; this in turn implied that no additional spoilers could be added (see above item), and that wakefields from the collimators were at the limit of tolerability
- A further consequence of interleaved collimation was that the horizontal collimation depth could not be adjusted independently of the energy collimation depth

- A further consequence of the strong wakefields was that IP-phase collimation was looser in the second iteration than FD-phase; this meant that the phase advance from the collimation system to the IP had to be carefully adjusted, both for on-energy and off-energy particles, lest an off-energy particle at large amplitude migrate from IP phase in collimation to FD phase in final focus; this required extremely careful control of the chromaticity of the beam delivery system.

Since the publication of the *ZDR* in 1996, a number of new developments have led to a new approach to the collimation system design. The first of these was an examination of the operation history of the SLC: while the SLC frequently experienced large oscillations in its beam delivery system due to energy errors or feedback hardware/software problems, large oscillations due to sudden catastrophic failure of a quadrupole magnet were quite rare – in fact, there is no documentation of a catastrophic magnet short occurring in an inter-pulse period. The second new development was that the architecture of the NLC machine protection system (MPS) matured, and it was clear that the NLC would require pulse-to-pulse orbit monitoring to protect the linacs from errant beams. As a consequence of these changes, it was decided that the NLC collimation system should provide passive protection against energy faults, which are likely to occur frequently and without advanced warning, but that betatron oscillations can generally be trapped by a combination of systems engineering (weak and/or slow feedback correctors and magnet movers, for example), orbit monitoring (to detect quadrupole shorts in progress), and judicious use of permanent magnets; thus the betatron collimators do not need to adhere to such a strict requirement of passive protection for all collimators.

Figure 2 shows the optical functions of the proposed new collimation system. The desirable features of the new system are:

- Separated collimation regions for energy and betatron offsets; the energy collimation system provides passive protection of its spoilers through large horizontal dispersion functions and vertical betatron functions, and protects its absorbers through MCS in the spoilers, while the spoilers in the betatron collimation system would not survive contact with a full bunch train.

- Both energy and betatron collimation provide two iterations of collimation per degree of freedom.

- The betatron collimation system has spoilers upstream of each absorber and equal collimation in both phases.

- The betatron collimation system absorbers have an aperture which is 3 to 5 times as large as the spoiler apertures

- The betatron collimation system absorbers can be made with a fixed aperture, which simplifies the system design and permits the use of round-aperture absorbers; the latter are expected to have a smaller wakefield kick than rectangular-aperture collimators

- The optics in all parts of the system are weaker than in the 1996 design.

- The total length is approximately 50% of the length of the 1996 design.

- The energy collimation lattice incorporates a pulsed kicker magnet (called a Single Beam Dumper, or "SBD", following the SLC notation) which can extract the beam downstream of the main linac energy diagnostic station; this permits linac commissioning without requiring the beam to pass through the IP.

In this Note we survey the physics issues which shaped the new design, describe the new design and its performance in detail, and estimate the scaling of the system as a function of various parameters, most notably CM energy.

2 Overview of Relevant Physics and Design Requirements

The principal physics concerns which shaped the new collimation system design are: the collimation requirements of the final focus (collimation amplitudes, halo population, and muon production), optical distortions which arise from the lattice, luminosity reduction due to collimator wakefields, and damage mechanisms/thresholds for the collimator jaws. Each of these issues is described below.

In order to permit flexibility of operation, the NLC parameter list describes an "operating plane," in which bunch charge, emittance, and betatron functions are varied to provide approximately constant luminosity [4, 5]; the parameters which are relevant to the collimation system are listed in Table 1. In addition, the NLC is designed to have considerable flexibility in its CM energy: the achievable range is expected to be from 92 GeV to 1 TeV. At this time the operating plane is defined only for the 500 GeV and 1 TeV CM energies. In order to have *ansatz* parameters to study at any desired CM energy, we assume the following:

- The present balance of bunch charge, bunch length, and IP normalized emittances shown in the 500 GeV and 1 TeV CM parameter lists are valid at all energies; this means, for example, that even for 92 GeV CM we will assume that the largest bunch charge will be 1×10^{10}, and that this charge will correspond to normalized emittances of 5×0.12 mm.mrad at the IP; the jitter and emittance budgets are similarly assumed to be valid for all CM energies.

- The IP betatron functions (β^*) for the 500 GeV and 1 TeV CM parameter lists are valid for all energies between 500 GeV and 1 TeV CM; thus, between these two energies the beam size and divergence scale with $1/\sqrt{E_{\rm CM}}$.

- For CM energies lower than 500 GeV, the IP betatron functions will be relaxed to preserve the IP angular divergences given by the 500 GeV CM parameter list; this implies that β^* scales with $1/E_{\rm CM}$, and that the 500 GeV CM divergences are at the limit of the acceptance of the final focus.

For each phenomenon considered, we use the parameter list in [4], the different emittance budgets for the different cases in the operating plane, and the rules above to determine the NLC operating situation for which the parameter is at its most severe. Emittance dilutions are always compared to damping ring emittances ($\gamma\epsilon_{x,y} = 3 \times 0.03$ mm.mrad) for consistency across the machine.

2.1 Collimation Amplitudes

The first question which must be answered definitively for the collimation section of a linear collider is, "How deeply do you have to collimate?", or equivalently, "How close do the collimators have to get to the beam to make the backgrounds low in the detector?" The most conventional sources of background from beam halo are primary beam particles and secondaries generated when primary beam particles hit apertures near the detector (indeed, the latter is the principal reason that collimation cannot be entirely performed close to the IP). These sources can be relieved by engineering: use of large-aperture magnets, masking inside the detector, elimination of unnecessarily tight apertures in the IR, etc. For electron beams at very high energy, there is an additional source: synchrotron radiation from bending and quadrupole magnets. The NLC final focus includes a soft

Table 1: NLC parameters of relevance to the collimation system. Note that BDS jitter must be added in quadrature with incoming jitter to estimate total beam jitter, in sigmas, at end of BDS.

Parameter	Units	500 GeV CM			1 TeV CM		
		A	B	C	A	B	C
Bunch Charge	10^{10}	0.7	0.82	1.0	0.7	0.82	1.0
Bunches/Train	–	95	95	95	95	95	95
Bunch Spacing	nsec	2.8	2.8	2.8	2.8	2.8	2.8
Bunch Length	μm	90	120	140	90	120	140
End-linac $\gamma\epsilon_{x,y}$	10^{-8} m.rad	360/5.25	405/7.2	435/9.6	360/5.25	405/7.2	435/9.6
IP $\gamma\epsilon_{x,y}$	10^{-8} m.rad	400/6.5	450/8.5	500/12	400/6.5	450/8.5	500/12
$\beta^*_{x,y}$	mm	12/0.12	12/0.12	13/0.15	12/0.12	12/0.15	13/0.15
$\sigma^*_{x,y}$	nm	310/4.0	330/4.6	365/6.2	220/2.8	235/3.2	260/4.4
$\theta^*_{x,y}$	μrad	26/33	28/38	28/40	18/23	20/24	20/28
Incoming jitter	sigmas	0.17 (x), 0.17 (x'), 0.44 (y), 0.44 (y'), 0.22% (Energy)					
BDS Jitter Budget	sigmas	0.1 (x), 0.1 (x'), 0.25 (y), 0.25 (y')					

bend upstream of the final doublet; this soft bend causes the SR fan from upstream magnets to be offset in x from the detector centerline, which permits masking of the SR. This leaves the SR from the final doublet magnets, which are too close to the IP to permit such masking and which are typically the strongest quads in the beamline. The trajectories of SR photons emitted in the final doublet are a function of the free distance between the last quad and the IP (L^*), the lengths and gradients of the final doublet magnets, and their separation. Thus, given the detector beampipe radius and final doublet optics, the SR swath from the doublet sets a limit on how loosely we are permitted to collimate the beam halo.

2.1.1 Betatron Amplitudes

Figure 3 shows the trajectory of SR photons emitted by particles with large horizontal and vertical offsets, respectively, in the present final focus optics with long (4.3 m) L^* [6], and the "LCD Large" detector. The rays in Figure 3 indicate that particles with horizontal IP angles less than 240 microradians (horizontal) by 1 milliradian (vertical) produce photons which do not hit within the detector. A full 2-dimensional study has indicated that the safe region in $x'^*y'^*$ is an ellipse with semi-minor axis equal to 300 microradians (x'^*) and semi-major axis equal to 1.2 milliradians (y'^*). Because our collimation will produce a rectangular beam halo, the collimation will have to be somewhat tighter than this. Rectangular collimation limits of 240 microradians by 1 milliradian appear to provide adequate protection of the detector from synchrotron radiation with a small margin to permit static misalignments.

The actual collimation amplitude has to be set somewhat tighter than the limits above would indicate. This is due to two phenomena. The first phenomenon is that some of the horizontal aperture must be reserved for the off-energy particles at the IP (see Section 2.1.2, below); we have assumed that ± 59 microradians is required for off-energy particles, which reduces the allowed betatron amplitude to ± 191 microradians. The second is the phenomenon of phase migration mentioned earlier. Figure 5 is a diagram of collimation in phase space using a system which has collimators every 90° in betatron phase. As shown in Figure 5, collimating a circumscribed rectangle at a given number of sigmas in xx' phase space does not eliminate a substantial number of particles

which are at larger amplitudes than the desired collimation depth. In order for such a scheme to work, the beam delivery system design must carefully place the final doublet in phase with one of the collimator jaws, and eliminate chromaticity in the intervening system (which would otherwise cause energy-dependent phase migration). To avoid such problems, the present design collimates an inscribed rectangle in phase space, as shown in Figure 6. This has the practical effect of requiring all collimation to be tighter than in Figure 5 by a factor of $\sqrt{2}$. Thus the collimation depth is ± 135 microradians in the horizontal and ± 707 microradians in the vertical, and these limits are a constant for all CM energies.

The IP angular divergences are largest at 500 GeV CM, as we have assumed that for lower energies the 500 GeV CM divergences are maintained; the largest divergences in horizontal and vertical are "Case C", with $\theta^*_{x,y} = 28 \times 40$ microradians. This means that we need to collimate at 4.8 σ_x by 17.7 σ_y at the worst (ie, tightest in sigmas) case. Such collimation depths should not be cause for alarm: both FFTB and SLC routinely collimated at the former, and the latter is quite loose by contemporary standards.

It is worth noting that the collimation gap size in *sigmas* and the gap size in *meters* do not scale the same way with energy. While the gap in sigmas is a constant for all energies below 500 GeV CM and then increases with energy from 500 GeV to 1 TeV CM, the gap in meters is constant from 500 GeV to 1 TeV CM and increases with $1/\sqrt{E_{\rm CM}}$ for lower energies.

2.1.2 Energy Depth

The collimation requirements for off-energy particles is set by two phenomena. The most immediate is the SR emission in the final doublet: since the present final focus design has a nonzero angular dispersion at the IP, off-energy particles have nonzero x'^* values, and the allowed range of x'^*, as discussed above is ± 240 microradians. The IP angular dispersion, η'^*, is 5.9 mrad [6]; thus, the energy collimation must be tighter than $\delta_{\rm max} = 240$ μrad/5.9 mrad, or $\pm 4.07\%$. In fact, the limit must be tighter than this, since the present collimation system transmits a five-dimesional parallelepiped to the IP: a particle with a large energy offset and a large horizontal position offset must be accomodated, and the prescription above would permit a particle with an energy offset of 4.07% and a betatron amplitude of $4.4\sigma_x$ to go to the IP and produce unacceptable SR. In order to ensure that a particle which simultaneously has the maximum betatron amplitude and maximum energy amplitude is within the safe region at the IP, we must set $\delta_{\rm max}\eta'^* + x'_{\rm max} = 240$ μrad, i.e., the amplitudes add linearly (not in quadrature). In order to ensure that a sufficient fraction of the ± 240 μrad is allocated to betatron amplitude, we have assumed that energy collimation is performed at $\pm 1\%$ off-energy.

The second phenomenon which contributes to the energy depth determination is the dynamic aperture of the beam delivery system as a whole. For particles at large amplitudes in betatron or energy degrees of freedom, the beam dynamics of the BDS can be quite different from the on-energy, near-axis optics (see Section 2.4, below). The second condition on the energy collimation depth, then, is that a particle with the maximum energy offset and maximum betatron amplitude transmitted by the collimators must not be "pushed out" of the safe envelope between the collimators and the IP.

2.2 Halo Population, Sources, and Distribution

The amount of beam power which populates the non-gaussian tails, and the distribution of that halo, are extremely difficult to estimate analytically. In the following sections we attempt such estimates. In addition, we can be guided by the SLC/SLD experience. Data taken during beam-based alignment of the SLD vertex detector with the SLC beam are consistent with a flat halo

containing on the order of 0.1% of the SLC beam. This is not a unique characterization of the halo, as many other distributions would also be consistent with the data.

2.2.1 Linac Wakefields, Mistuning, Nonlinearities

The NLC main linacs are less dominated by wakefields than the SLC linac was; this is due to careful design of the optics to ensure that the head-tail energy difference required to achieve "autophasing" (the condition at which, to lowest order, the chromaticity of the linac cancels the wakefields) is small enough to be reasonably achieved – on the order of 1%, rather than the SLC's 6%.

Nonetheless, wakefields can play a role in generation of a beam halo. A simulation study of a beam passing through the main linac with a $20\sigma_y$ initial offset indicated that such a large betatron oscillation could potentially drive approximately 10^7 particles per bunch train into the tails. It is important to note that, in this case, the luminosity degradation was almost total – thus this is not a condition in which we expect to run routinely.

2.2.2 Dark Current

A substantive study of dark current capture in the NLC main linac has not been performed. However, such a study has been performed for the TESLA superconducting 1.3 GHz main linac [7]. The TESLA study assumed 1 μA of dark current per 9-cell cavity (approximately 1 μA per meter of accelerating structure), a main linac with injection energy of 3 or 5 GeV and a phase advance of 60° per cell in each plane, and also made certain assumptions about the phase volume and distribution of the dark current beam. The study found that the expected dark current halo which was transported to the 250 GeV end of the linac was approximately 4×10^7 particles for 3 GeV injection energy and approximately 2×10^4 particles for 5 GeV injection energy. Because the dark current is so low in energy (typical particles are 11 MeV), only the halo generated near the low-energy end of the lattice can survive the over-focusing of the main linac quads.

The NLC main linac injection energy is 8 GeV, and the focusing of the NLC lattice is stronger than that in the TESLA lattice. We therefore expect a smaller fraction of the linac dark current to be transported to the collimation system. In the absence of a more conclusive study we tentatively assume that the NLC dark current halo will be comparable to that of TESLA, while noting that such a study should be performed for NLC as soon as possible.

2.2.3 Beam-Gas and Thermal Photon Scattering – Linac

One source of beam halo that has been identified in recent years is primary beam particles scattering off of residual gas in the accelerator or photons associated with blackbody radiation [8, 9, 10]. A recent calculation of the number of halo particles generated in the NLC main linacs from thermal-photon scattering, beam-gas Bremsstrahlung, beam-gas Coulomb scattering, and atomic-electron scattering indicates that fewer than 10^4 such particles will be generated per 10^{12} primary beam particles [11].

2.2.4 Beam-Gas and Thermal Photon Scattering – BDS

The study of primary-beam scattering in the Beam Delivery System is considerably more complex than the equivalent study in the linac for several reasons:

- Because of the unusual optics in the final focus – immense betatron functions in the final doublet phase and miniscule ones in the interaction point phase – collimation in the final focus is only possible at the final doublet phase

- The large betatron functions in the final doublet phase imply that small scattering angles will cause primary beam particles to leave the beam core, but particles that scatter in the doublet phase cannot cause backgrounds
- Particles which scatter in the final doublet phase which are off-energy due to the natural energy spread of the beam or due to inelastic scattering processes can undergo phase migration and wind up with a large amplitude in the final doublet phase.

A previous study of scattering in the *ZDR*-era beam delivery system [10] determined that fewer than 2000 particles would be lost due to scattering processes if a base pressure of 10^{-8} Torr was achieved. The present beam delivery system is likely to have even fewer lost particles than the original design due to its comparatively relaxed optics, reduced length, increased vacuum chamber aperture (permitting a lower base pressure) and improved optical linearity in the final focus. On the negative side, the present design has fewer ideal locations for collimation far from the IP. While we believe that the earlier study implies that backgrounds from scattering in the beam delivery system itself will not be a critical issue, this study should be revisited in the near future.

2.2.5 Injector

A likely source of beam halo is the injector systems: the linacs upstream and downstream of the damping rings, the damping rings and their transport lines, and the first bunch compressor. During the SLC era, the damping rings and their transport lines were considered a likely candidate for the prime beam halo source [12]. The amount of halo from these sources is difficult to estimate. However, the NLC will have an advantage which the SLC did not: a 5-dimensional collimation system at the 8 GeV point (directly upstream of the turnaround which begins the second bunch compressor), where the beams are large and the stored energy in a bunch train is small, which will remove this halo before it is accelerated to full energy. If we assume that the injectors produce 10^{11} halo particles per bunch train (equivalent to 10% of the beam power – a very pessimistic estimate), and the collimation system at the 8 GeV point has approximately 1% transmission of halo (also a very pessimistic estimate), then the beam halo contribution from the injectors will be 10^9 particles per train, or 0.1%. A more sensible estimate might be that the halo will be 1% of the beam power and that the collimation system transmission will be on the order of 10^{-4}, which leads to a sensible injector halo estimate of 10^6 particles per bunch train.

2.2.6 Summation

At the present time we have identified potential mechanisms for producing a halo population of roughly 10^7 particles per bunch train. In order to achieve this population it is necessary to mistune the main linac to such a degree that the luminosity is almost totally degraded.

In some cases our calculations of potential halo sources are in their infancy. In addition, SLC experience indicates that a considerable engineering margin is potentially desirable for the collimation system. We therefore have elected to use an approximate halo figure of 10^9 particles per bunch train as the estimate in our designs and studies of the system. It is important to note that the collimation system design would probably not change dramatically even if we were to be convinced that there will be no halo, since the machine protection role of the system is the principal driver. Two changes that would likely be made if the halo population was dramatically below our expectations are: removal of muon spoiler magnets (discussed below), and relaxation of the betatron collimation depth in order to ease single-bunch wakefield concerns.

2.3 Muons from Collimation

When high-energy electron beams encounter a thick target such as a collimator, a fraction of the beam energy is converted to relativistic muon secondaries. Muon secondaries are a potentially significant source of detector backgrounds because the muon energy spectrum approaches the primary beam energy and because muons can travel for tens or even hundreds of meters through dense solids. At the startup of SLC, muons were a signficant source of background; a program to reduce this background caused a delay in physics running. The physics of muon secondaries – their production, transport, and impact on the detector – pose a potentially fundamental limit on the amount of beam halo which can be safely removed in the collimation system.

In order to understand the relationship between collimation and muon backgrounds, we simulate muon production at several z locations in the NLC beam delivery system tunnel (assumed in this design to be straight from the linac to the IP), and simulate the transport of muons to the "Large" detector endcap. As a figure of merit, we determine how many collimated electrons are required at a given z location to generate one muon which passes through the detector endcap. Figure 4 shows this ratio as a function of z for 250 and 500 GeV beam energies. We consider two beamline configurations: an empty tunnel, and a tunnel which contains two "tunnel-filler" iron muon spoilers which are magnetized to deflect secondaries away from the detector (in this case there is a 9 meter long spoiler approximately 900 meters upstream of the IP, and an 18 meter long spoiler approximately 300 meters upstream of the IP). Figure 4 indicates that a system with no muon spoilers has at least 3 orders of magnitude more muons hitting the detector per bunch train than a system with 2 spoilers.

The muon background acceptance of the NLC detector is impossible to quantify at this time. We can, however, use Figure 4 to quantify how many muons the detector will see: for 500 GeV CM, 1×10^9 electrons collimated per bunch train, and 2 muon spoilers as described above, the detector will see on the order of 1 muon per train from each side of the IP, while at 1 TeV CM this number will increase to a few tens of muons per side per bunch train. The number of muons increases 2-3 orders of magnitude without the spoilers. Our baseline design, therefore, is to continue to plan for up to 1×10^9 particles collimated in the halo and to use the 2 spoilers described above. If the muon backgrounds become unacceptable as the CM energy is increased from 500 GeV to 1 TeV, we will seek to add incremental improvements such as a third spoiler per side to remedy the situation.

2.4 Optical Distortions

The principal optical distortions which appear in systems such as the collimation system are an assortment of chromatic aberrations. These can be very generally divided into three categories:

- Various orders of *dispersions*, which are correlations between transverse position and energy. These dispersions are generated by bend magnets; in addition, low-order dispersions can interact with higher-order optics (sextupoles, octupoles, or the chromaticity of quadrupoles, see below) to generate high-order dispersions. The linear dispersions ($R_{16,26}$, or η_x, η'_x) and second-order dispersions ($T_{166,266}$) can usually be driven to zero at the end of a bending system by careful design; higher-order dispersions (such as U_{2666} or V_{16666}) can be more difficult to control. Because the NLC collimation system has only horizontal bending, no vertical dispersions are present at any point in the system. Dispersions of all orders are not functions of beam emittance, and thus a study of dispersion at a single emittance can be easily generalized to other emittance values.

- Various orders of *chromaticity*, which are correlations between linear focusing and energy. Chromaticity is generated by quadrupoles or by sextupoles in a dispersive region, and low-

order chromaticities can interact with one another to produce high-order chromaticities. Typical chromaticity matrix elements have two geometric indicies, both in the same plane (such as T_{216}, or U_{4366}). Like dispersions, the relative impact of a given chromaticity is not a function of emittance.

- *Chromo-geometric aberrations* are interactions of chromaticities with geometric aberrations; their matrix elements include more than two geometric indicies, which need not be all in one plane, for example U_{1446}; they may also include two unmatched geometric indicies, for example U_{1466}. Chromo-geometric aberrations are a function of emittance: a larger geometric emittance will experience a larger fractional dilution than a small one. Chromogeometric aberrations typically occur in systems which have of strong nonlinear magnets in regions of high chromaticity (for example, the two terms listed above were present in the SLC final focus original design [13]; consequently systems which are suspected of having strong chromo-geometric aberrations must be studied for several different emittances.

The effect of chromatic aberrations is typically summarized by measuring the range of energies over which a system produces acceptably well-matched beams at its output, also known as the system *bandpass.*

A less-common optical distortion is a purely geometric aberration, which causes emittance dilution for even a monochromatic, on-energy beam. These aberrations are relatively common in storage rings (which have large numbers of interleaved sextupoles) and linear collider final focus systems (which have a small number of extremely strong sextupoles, and often octupoles or decapoles as well), but are not common for transport lines (although the SLC damping ring RTL's are a notable example of a transport line with substantial geometric aberrations) [14].

A third optical distortion of interest in this system is horizontal emittance dilution due to synchrotron radiation. The growth in normalized emittance due to bend magnet synchrotron radiation is given by [15]:

$$\Delta\gamma\epsilon_x = 4 \times 10^{-8}\text{m.rad} \cdot E^6[\text{GeV}]I_5, \tag{1}$$

where I_5 is the fifth synchrotron radiation integral [16]:

$$I_5 = \int dz \frac{\eta^2 + (\eta'\beta + \eta\alpha)^2}{\beta|\rho|^3}. \tag{2}$$

Equations 1 and 2 indicate that, for a given lattice of given length, the synchrotron radiation emittance growth increases as the sixth power of the beam energy and the fifth power of the bending fields (two powers from the dispersions in the numerator, three from the radius of curvature in the denominator). It can also be shown that, for a given desired dispersion function in a lattice, the emittance dilution is inversely proportional to the system length to the fifth power. Thus in general,

$$\Delta\gamma\epsilon_x \propto \frac{E^6\eta^5}{L^5}. \tag{3}$$

2.5 Collimator Damage Issues

In order to accomplish the goals of halo removal and machine protection, it is necessary for the post-linac collimators to approach the beam core more closely (in units of beam sigma) than any other aperture. This in turn implies that the design of the collimators must include consideration of the mechanisms and thresholds for beam damage of the collimators.

In the present design, both the energy and betatron collimation lattices use a variation on the spoiler/absorber scheme presented in the *ZDR* [3]. The spoilers in the betatron collimator are

"consumable," and can therefore tolerate a certain amount of damage before requiring replacement (see Section 3.2), while the energy collimation spoilers and all absorbers must be designed to withstand relatively frequent contact with a single errant bunch train.

The principal criterion for collimator "damage" is that the surface finish near the beam is irreversibly degraded to such an extent that it increases the effect of transverse wakefields (see Section 2.6, below). The principal mechanism for such damage is assumed to be instaneous heat deposition into the material. Three sources for such heating have been considered: electric field breakdown, image current heat deposition, and direct ionization (i.e., electrons passing through the material).

2.5.1 Collimator Damage and Instantaneous Heating

All of the collimators in the NLC post-linac collimation system must be capable of tolerating the steady-state heat load of a well-behaved beam indefinitely without being damaged; in addition, the betatron collimation absorbers, the energy collimation absorbers and the energy collimation spoilers must be capable of withstanding the heat load of a single errant bunch train without being damaged.

At this time there is no analytic method for deterimining with high precision the instantaneous temperature rise which will cause a collimator made from a given material to fail, since the number of significant unknowns in the problem is large. A reasonable estimate of the maximum allowed temperature rise can be obtained by considering a fully-constrained piece of material which experiences a sudden increase in temperature. Since the heated material is fully constrained, it is unable to expand; therefore the thermal expansion of the material must be cancelled by pressure exerted by the surrounding material. When the pressure required for this cancellation exceeds the ultimate tensile strength of the material, it can be expected to fail, thus:

$$\Delta T_{\rm fail} \alpha_T E_{\rm Young} = 1.5U, \tag{4}$$

where $\Delta T_{\rm fail}$ is the instantaneous temperature rise which causes mechanical failure, α_T is the coefficient of thermal expansion, $E_{\rm Young}$ is Young's modulus, and U is the ultimate tensile strength of the material. The factor of 1.5 in Equation 4 is due to the fact that the heating occurs too quickly for crack propagation. Equation 4 gives an estimate of the failure temperature which is in general lower than the melting point and thus more conservative. A third limit is given by material vapor pressures: if the CW heat load is sufficient, the vapor pressure of the collimator at its elevated operating temperature will be high enough to evaporate the surface during the course of a run. This limit is also typically higher than the fracture temperature, and is always too high to be a comfortable limit. Thus, for our purposes we take the fracture temperature, as defined in Equation 4, to be the limit for instantaneous temperature rise of a collimator. Table 2 shows the relevant properties of several prospective collimator materials. Note that, in addition to the temperature rise, the allowable energy deposition (in joules per cubic meter) must also be considered.

Note that the analysis which led to Equation 4, while probably reasonable for a thick piece of material (such as an absorber) is probably a severe underestimate of the allowable temperature for a thin piece of material (such as a spoiler). This is because for a spoiler the assumption of full constraint is not accurate; The material is permitted to expand at the surfaces and thus the surrounding material does not need to apply force to counteract the entirety of the thermal expansion [17]. In "death ray" tests of copper and other materials, it was found that even when the instantaneous heating was an order of magnitude larger than Equation 4 would indicate, damage was confined to the region of the beam core and no cracking was seen [18]. Nonetheless, we can

Table 2: Thermal damage parameters for prospective collimator materials. Sources: [19, 20, 21, 22]. Expansion coefficient and Young's modulus for alloys assumed to be the same as values for the dominant material. "Tensile strength" and "ultimate tensile strength" used interchangably. Carbon values refer to commercially-available, non-porous "glassy carbon."

Material	Expansion Coeff,$10^{-6}/°$C	Young's Modulus, GPa	Tensile Strength, MPa	Max ΔT,°C	Max MJ/m^3
Beryllium	11.5	318	600	250	840
Carbon	1.1	35	580	2260	3800
Titanium	8.7	120	370	530	1260
Ti alloy	8.7?	120?	1100	1580	3750
Copper	16.6	130	216	150	510
Iron	11.9	211	340	200	710
Steel	11.9?	211?	800	480	1700

use the values in Table 2 as a general indicator of the suitability of a material or the riskiness of an installation.

In the case of steady-state heat load, the collimators must resist damage due to metal fatigue from continual thermal cycling as well as damage due to instantaneous single-pulse heating. The former limit is actually the more restrictive: while copper is believed to be capable of surviving occasional instantaneous temperature rises of 150°C, recent experiments have indicated that fatigue damage can occur due to 10^8 cycles of 120°C [23]. In this Note, we will assume that the fatigue temperature limit is 10% of the single-pulse damage limit in Table 2.

As mentioned above, there are three sources of collimator damage that we have considered. Each one is briefly described below; in calculations the bunch charge is assumed to be 10^{10} particles, with an approximate RMS length of 100 micrometers or 330 femtoseconds.

Electric Field Breakdown: This is a collective effect, due to the high charge in a single bunch. A sufficiently high electric field will "pull a spark" from the collimator, resulting in heat damage due to the spark moving through the resistive material and/or bremmstrahlung. A straightforward application of the integral form of Gauss' law indicates that the peak electric field from the bunch a radial distance r from the center is on the order of 10^5 V/r. For a collimator jaw 100 μm from the beam this is on the order of 1 GV/m. It is believed that a smooth metal surface can tolerate such a high field for the short time that the bunch is exciting the surface of the collimator.

Image Current Heating: This is also a collective effect: when the beam passes through the aperture of the collimator, it generates image currents which flow on the resistive surfaces of the collimator jaws, leading to so-called "I^2R" heating.

The pulsed heating of a metal surface from image currents has been estimated for a beam which is centered in a round pipe of radius r [24], and we make the assumption that the case of a beam centered in a rectangular collimator of half-gap r is comparable. The energy density deposited by a bunched beam of charge Q and RMS length of σ_z is given by:

$$E_D = \frac{Z_0 c}{2\pi}\frac{Q^2}{\sigma_z^2}\frac{1}{4\pi^2 r^2}. \tag{5}$$

In the case where the beam is near the collimator jaw but still far enough away to be considered pointlike (i.e., $\sigma_{x,y} \ll r \ll r_1$), the maximum deposited energy density is a factor of 4 larger than the value indicated in Equation 5. For a beam which is so close to the collimator jaw that particles

from the beam are beginning to penetrate the material, the maximum energy deposition is given by:

$$E_D = \frac{Z_0 c}{2\pi}\frac{Q^2}{\sigma_z^2}\frac{f_{\max}^2(\sigma_y/\sigma_x)}{\pi^2\sigma_x\sigma_y}, \tag{6}$$

where it is assumed in Equation 6 that the collimation is occurring in the vertical plane and not the horizontal, and the function $f_{\max}$ is given approximately by:

$$f_{\max}(v) \approx \sqrt{\frac{1}{2\pi}}\frac{\ln(1+\pi v)}{\sqrt{v}}. \tag{7}$$

Equation 6 does not include the heat deposition due to beam-matter interaction, and should only be used as an estimate of the upper limit of image-current heating. Equation 6 can be combined with Equation 5 and the caveat about near-wall heating above to deduce the beam-collimator distance at which the energy deposition saturates.

In addition to the single-bunch temperature limit, the effect of the full bunch train must also be considered. As shown in [24], the crucial issue for multi-bunch heating is whether the heat deposited by the first bunch has diffused into a region of the collimator much larger than the area it was deposited into before the last bunch of the train has arrived. The diffusion distance is given by:

$$y_{\text{heat}} = \sqrt{K t_{\text{train}}/C_p}, \tag{8}$$

where K is the thermal diffusion coefficient of the material, C_p is the specific heat, and t_{train} is the duration of 1 bunch train in time. The heat is deposited in a layer of material with a characteristic depth δ_e, the "effective skin depth:"

$$\delta_e \equiv \Gamma(3/4)\sqrt{2\rho\sigma_z/c\mu}, \tag{9}$$

where ρ is the resistivity of the collimator surface, σ_z is the RMS bunch length, and μ is the magnetic permeability of the collimator surface, all in MKS units. As Table 3 shows, in all cases $y_{\text{heat}} > \delta_e$. In this case, a reasonable estimate of the multi-bunch deposited energy density is given by:

$$E_D(\text{train}) = E_D(1) N_p \frac{\delta_e}{y_{\text{heat}}\sqrt{\pi}}, \tag{10}$$

where $E_D(1)$ is the single-bunch deposited energy density, N_p is the number of bunches in 1 bunch train, and all other variables are as defined previously. Note that in the case where δ_e is comparable to y_{heat}, Equation 10 gives an overestimate of the energy deposition. Table 3 shows the relevant single- and multi-bunch parameters for image current heating. In the table, the minimum single-bunch and multi-bunch gap sizes assume that the threshold for fatigue damage is a temperature rise which is 10% of the single-pulse limit listed above.

Beam-Matter Direct Interaction: This is a single-particle effect, the result of the primary beam passing through the collimator material. The kinetic energy of the primary particle is converted to a shower of photons and electron-positron pairs; for primary beam energies above a few tens of MeV, the process is strongly dominated by bremmstrahlung rather than direct ionization of the material. In addition to the energy loss from bremmstrahlung, the particle undergoes elastic multiple coulomb scattering which results in a change in direction of the primary particles (essentially the angular divergence of the beam grows as it passes through the material). The two phenomena are to good approximation independent, with the result that the energy loss of a primary beam particle is not correlated to its scattering angle. We take advantage of the coulomb scattering property to enlarge the beam before it encounters the main energy-absorbing collimator

Table 3: Collimation system parameters related to image current heating of the collimators. Single-train parameters assume 2.8 nsec bunch spacing and 95 bunches per train.

Material	Min half-gap (1 bunch)	δ_e	$y_{\rm heat}$	Min half-gap (1 train)	Single-Pulse Damage Limit (1 bunch)	(1 train)
Beryllium	37 μ	179 nm	3.97 μ	58 μ	23 μ	37 μ
Carbon	17 μ	3.31μ	1.03 – 19.2 μ	51 – 220 μ	11μ	32 – 140 μ
Titanium	30 μ	578 nm	1.56 μ	134 μ	19 μ	85 μ
Ti alloy	17 μ	578 nm	1.56 μ	76 μ	11 μ	48 μ
Copper	48 μ	115 nm	5.56 μ	51 μ	30 μ	32 μ
Iron	41 μ	278 nm	2.46 μ	101 μ	26 μ	64 μ
Steel	26 μ	278 nm	2.46 μ	64 μ	16 μ	40 μ

(this is the essence of the spoiler/absorber scheme); the energy loss of the beam is a purely negative consequence of collimation that must be adequately managed.

Electromagnetic showers in matter are usually characterized by the *radiation length* of the material, designated X_0 and defined as the e-folding distance for the energy of the primary beam particle as it passes through the target. Let us define the variable t as the distance into a given target in units of radiation length, e.g. $t \equiv x/X_0$; the energy loss of the primary beam can therefore be written simply as $dE/dt = -E$, or $E = E_{\rm beam}e^{-t}$. Both the bremmstrahlung and the coulomb scattering processes are stochastic. The azimuthal scattering angle obeys a Gaussian distribution with RMS angle given by:

$$\sigma_{theta} \approx 2.12 \times 10^{-2} \frac{\sqrt{t}}{E_{\rm beam}}. \tag{11}$$

The energy distribution of the primary beam after bremmstrahlung is given by [25]:

$$\frac{dN}{N} \approx d\delta \frac{1}{\Gamma(t/\ln 2)} \left[ln\left(\frac{1}{1+\delta}\right)\right]^{(t/\ln 2 - 1)}. \tag{12}$$

So much for the distributions of the primary beam: what of the energy deposition into the target? This is a very complicated problem due to all of the possible paramters involved (thickness of the target in meters, thickness in radiation lengths, incoming size and divergence of the primary beam, etc.); exact solutions for given geometries are usually obtained by simulations. Figure 7 shows dE/dt as a function of t for several materials which are candidates for collimators, based on EGS simulations; the units of dE/dt are joules per radiation length per incident electron.

For either thin or thick targets, the peak energy density deposition by the beam-matter interaction is given by:

$$E_D = \frac{dE}{dt}\frac{1}{X_0}\frac{1}{2\pi\sigma_r^2}, \tag{13}$$

where σ_r is the RMS beam size for a round beam (for a flat beam $\sqrt{\sigma_x\sigma_y}$ may be substituted). Table 4 shows the minimum beam sizes tolerable on thin and thick targets made from various materials if the target is to survive 10^{12} particles incident at 500 GeV per beam.

2.6 Wakefield Issues

One of the principal issues of the NLC post-linac collimation system is the effect of wakefields on the beam dynamics. The main concern is with the transverse, dipole-mode wakefields operating

Table 4: Minimum RMS beam size tolerable by targets of various materials, various thicknesses. The zero-thickness beam size is the size required for a coating on the front face of a collimator jaw to survive the beam passage. Iron/steel energy density deposition is assumed to be identical to copper. Bunch-train charge of 10^{12} electrons at 500 GeV per beam is assumed.

Material	X_0, cm	0.0 X_0	0.5 X_0 Target	1.0 X_0 Target	20 X_0 Target
Beryllium	37.5		185 μ		300 μ
Carbon	20.1	45 μ	76 μ	105 μ	123 μ
Titanium	3.7	120 μ	180 μ	300 μ	750 μ
Ti alloy	3.7	70 μ	100 μ	170 μ	440 μ
Copper	1.5	275 μ	470 μ	760 μ	2.7 mm
Iron	1.8	210 μ	360 μ	590 μ	2.1 mm
Steel	1.8	140 μ	230 μ	380 μ	1.3 mm

over a short range (typically within a single bunch of the bunch train), although higher-order mode wakefields will also be considered.

There are three sources of wakefields which are considered relevant to the collimation system:

- The deflecting fields caused by changes in the cross-sectional dimensions or shape of the vacuum chamber, typically known as *geometric wakefields*
- The deflecting fields caused by the finite resistivity of the vacuum chamber, typically known as *resistive-wall wakefields*
- The deflecting fields due to surface features on the vacuum chamber, typically known as *surface-roughness wakefields*.

All of the sources of transverse wakefields were encountered in the SLC's end-of-linac collimation system. Based on that experience, our intention is to minimize the transverse wakefields by using tapered collimators to reduce the geometric effects, using high-conductivity materials where possible to mitigate the resistive-wall effects, and using smooth collimators to mitigate the impact of surface finish. It is primarily the latter phenomenon which puts strict limits on the amount and types of surface damage which the spoilers may tolerate.

The NLC post-linac collimation system has three distinct types of collimators:

- Adjustable-jaw spoilers: these are optically thin devices with a rectangular aperture, used in both betatron and energy collimation sections
- Adjustable-jaw absorbers: these are optically thick devices with a rectangular aperture, used only in the energy collimation section; because they have a long untapered region at minimum aperture, these devices have a larger resistive-wall wakefield than a comparable spoiler
- Fixed-aperture absorbers: these are optically thick devices with a round aperture, which are used as halo absorbers in the betatron collimation section and as a protection device in both energy and betatron sections.

In the next section we present the basic equations and "rules of the road" for tapered collimators, which are then converted into more useful forms in the subsequent sections.

2.6.1 Basic Equations

Near-Center Wakefield: The near-center wakefield, which deflects the centroid of the beam when it is offset from the center of the collimator by a distance small compared to the collimator gap, is the omnipresent beam dynamics issue of all the collimators in the NLC. The near-center wakefield results in amplification of the incoming jitter: a position jitter at the collimator results in an angle kick, which means that some additional angle jitter is generated from the position jitter at the collimator. Furthermore, the deflection of the bunch is not uniform in z, which means that some emittance dilution is generated as well.

The analytic expression for the centroid deflection of a bunched beam through a tapered circular collimator is given by [28]:

$$y'_{\rm round} = \frac{1}{\sqrt{\pi}} \frac{N r_e}{\gamma} \frac{(r_0 - r_1)^2}{\sigma_z L_T r_0 r_1} y_0, \tag{14}$$

where N is the bunch population, $r_e = 2.8 \times 10^{-15}$ m is the classical electron radius, γ is the relativistic factor, r_0 and r_1 are the minimum and maximum aperture radius of the collimator respectively, L_T is the taper length (the full length of the element is $2L_T$), σ_z is the RMS bunch length, and y_0 is the position offset of the beam from the collimator symmetry axis. A similar expression has been derived for a rectangular-aperture collimator [29]:

$$y'_{\rm rect} = \frac{\sqrt{\pi}}{2} \frac{N r_e}{\gamma} \frac{h(r_0 - r_1)(r_0^2 - r_1^2)}{\sigma_z L_T r_0^2 r_1^2} y_0, \tag{15}$$

where terms are defined as in Equation 14 and h is the half-width of the collimator (i.e., the horizontal half-width of a collimator which cuts particles in the vertical). Note that Equation 15 is applicable only for shallow tapers ($r' \ll 1$), and for collimators in which the ratio r_1/h is less than the taper angle $\theta_T \equiv (r_0 - r_1)/L_T$. The deflection due to the resistive-wall wakefield of a regular cylindrical pipe of length L and aperture radius r_1 is given by [30]:

$$y'_{\Omega} = \alpha_G \frac{\Gamma(0.25)}{\sqrt{2\pi^3}} \frac{N r_e L}{\gamma r_1^3} \sqrt{\frac{c}{\sigma_z \sigma}} y_0, \tag{16}$$

where c is the speed of light and σ is the surface conductivity in inconvenient Gaussian units (equal to the convenient MKS conductivity multiplied by 9×10^9); α_G is a geometric form factor equal to 1 for a right circular cylinder and equal to $\pi^2/8$ for a rectangular vacuum chamber. Appropriate manipulation of Equation 16 produces an expression for a tapered collimator of circular or rectangular geometry:

$$y'_{\Omega} = \alpha_G \frac{\Gamma(0.25)}{\sqrt{2\pi^3}} \frac{N r_e L_T}{\gamma} \sqrt{\frac{c}{\sigma_z \sigma}} \frac{r_0 + r_1}{r_0^2 r_1^2} y_0. \tag{17}$$

Again, Equation 17 uses L_T for the length of one of the two tapers in the element, and the element length is given by $2L_T$. The deflection due to surface roughness is given approximately by [31]:

$$y'_{\rm rough} = \frac{4}{3\pi^{3/2}} \frac{N r_e L}{\gamma} \frac{1}{\sigma_z r^3} a f \alpha_s \, y_0, \tag{18}$$

where a is the characteristic size of the features, f is a form factor for the shape of the features which is typically between 1 and 20, α_s is the fraction of the surface filled with the features. An appropriate form of Equation 18 for tapered surfaces is:

$$y'_{\rm rough} = \frac{4}{3\pi^{3/2}} \frac{N r_e L_T}{\gamma} \frac{r_0 + r_1}{\sigma_z r_0^2 r_1^2} a f \alpha_s \, y_0. \tag{19}$$

Because the deflection of the bunch is not uniform in z, the beam angular divergence is also increased at the collimator jaw. For round or rectangular collimator jaws, geometric or resistive wakefields, the RMS increase in angular divergence is 40% of the mean centroid kick; this must be added in quadrature with the incoming divergence to determine the net effect on the beam quality. Note that the simple addition in quadrature is not exactly correct if the beam has a strong position-angle correlation, but in the present design the collimator jaws are typically at or near $\alpha = 0$ points so the naive quadrature addition above is an excellent approximation of the actual strength of the effect.

Near-Wall Wakefields: As the beam moves further from the center and towards one of the jaws of the collimator, the wakefield kick ceases to be a linear function of the beam position. The kick can become quite large, to the point where the near-wall wakefield is a potential machine protection issue. Because all of the circular aperture collimators in the system have much larger apertures than the rectangular aperture devices, we confine our consideration of the near-wall wakefield to the former category.

The near-wall centroid kick of a tapered rectangular collimator is believed to be [29]:

$$y' = \frac{2}{\sqrt{\pi}} \frac{N r_e}{\gamma \sigma_z} \frac{r_0 - r_1}{L_T} \ln\left(\frac{r_0 - y_0}{r_1 - y_0}\right). \tag{20}$$

Note that Equation 20 does not indicate any dependence of the deflection on h, which is qualitatively different from Equation 15. The deflection due to the surface resistance of a collimator or vacuum chamber is [34]:

$$y' = \alpha_G \frac{\Gamma(0.25)}{(2\pi)^{3/2}} \frac{N r_e L}{\gamma} \sqrt{\frac{c}{\sigma_z \sigma}} \frac{v + \sin v}{r^2 \cos^2(v/2)}, \tag{21}$$

where $v \equiv \pi y_0 / r$ and all other parameters are as defined in Equation 16. Note that in the limit $y_0 \ll r$, Equation 21 reduces to Equation 16. In its present form, Equation 21 describes the effect of an untapered vacuum chamber of flat or round geometry; an appropriate equation for describing a tapered vacuum chamber is left as an exercise to the reader[1].

Equations 20 and 21 both diverge as y_0 approaches r_1. As noted in the ZDR, however, the divergence is modified by the non-zero size of the beam in the uncollimated plane (for example, the horizontal size of the beam in a vertical collimator jaw) [35]. In this limit the beam resembles an infinite plane of charge (which has a nondiverging electric field) rather than a point of charge (which has a diverging electric field). For a vertical collimator, the deflection becomes saturated when $y_0 - r_1 \approx \sigma_x/2$. Another limitation is that the beam size is large in the plane being collimated; as the beam centroid approaches the collimator edge, therefore, some fraction of the beam particles are passing through the body of the collimator itself. The physics of this situation is unclear at this time; however, there are arguments that suggest that the particles which are passing through the collimator body do not participate in the generation of wakefields [36]. This means that both the effective charge of the beam (the charge which actually participates in the generation of wakefields) and the effective offset of the beam from the collimator wall are modified, as shown schematically in Figure 8. Figure 9 shows the change in effective offset and charge as a Gaussian beam passes close enough to a collimator that a fraction of the beam penetrates the material.

Quadrupole Wakefields: A beam which passes on-axis through a collimator can excite a quadrupole-mode wakefield, which will cause the beam to experience transverse focusing effects. The mean focusing of the collimator on the beam can be cancelled by adjusting the strength of a nearby magnetic quadrupole, but the quadrupole wakefield produces focusing which is not uniform in z, in the same way that the transverse deflection of the dipole-mode wakefield is not uniform

[1] Or a more mathematically-inclined coauthor.

in z; the RMS focusing error over the length of the bunch results in an increase in the emittance which cannot be tuned out by magnetostatic quads.

The quadrupole wakefield of a tapered collimator with rectangular aperture is given by [29]:

$$y' = \frac{2}{\sqrt{\pi}} \frac{N r_e}{\gamma} \frac{(r_0 - r_1)^2}{\sigma_z L_T r_0 r_1} y, \tag{22}$$

where y is the particle offset from the center of the collimator, and the beam centroid is assumed to be on-axis in the collimator. Note that Equation 22 is smaller than Equation 15 by a factor of approximately $2r_1/h$. Equation 22 is only valid for $y \ll r_1$; we follow the treatment in the *ZDR* and assume that at $y = r_1$ the kick is approximately twice the value estimated in Equation 22. The quadrupole wakefield of a rectangular collimator due to surface resistance is given by [37]:

$$y' = 4\alpha_G \frac{\Gamma(0.25)}{(2\pi)^{3/2}} \frac{N r_e L}{\gamma} \sqrt{\frac{c}{\sigma_z \sigma}} \frac{\sin u - u \cos u}{r^2 \sin^2 u}, \tag{23}$$

where $u \equiv \pi/2\ y/r$, y is the particle offset from the center of the collimator, and the beam centroid is assumed to be on-axis. Note that Equation 23 does not diverge as $y \to r$.

In the case of a circularly-symmetric tapered collimator, an on-axis beam generates a quadrupole wakefield only if the beam itself has a quadrupole moment [38]. The kick experienced by a test particle a distance y from the axis of a tapered circular collimator, assuming that the beam centroid is on-axis and $r_0 \gg r_1$, is given by [28]:

$$y' = -\frac{4}{9\sqrt{\pi}} \frac{N r_e}{\gamma} \frac{r_0}{L_T} \frac{\sigma_x^2 - \sigma_y^2}{r_1^3} y, \tag{24}$$

where σ_x and σ_y are the beam RMS sizes in the collimator. Equation 24 indicates that the quadrupole kick is weaker than the dipole kick by a factor of $4/9\ (\sigma_x^2 - \sigma_y^2)/r_1^2$. Note that, for fixed optical functions and normalized emittances, Equation 24 predicts that the deflection angle is inversely proportional to the second power of the energy.

2.6.2 Optimal Taper Angle

Let us assume that our tapered collimators have a gap size which is small compared to the aperture of the standard vacuum chamber size in the area, or in other words $r_0 \gg r_1$. In this case, we can rewrite Equations 14, 15, and 17 to replace terms of the form r_0/L_T with θ_T, the taper angle of the collimator. The kicks due to geometric wakefields in Equations 14 and 15 are proportional to θ_T, while in Equation 17 the kick is inversely proportional to θ_T. Assuming that the two kicks simply add linearly, therefore, we can find a value of θ_T which minimizes the near-center wakefield kick. A collimator with a rectangular gap has an optimal taper angle given by:

$$\theta_{\rm opt}^2 = \frac{\Gamma(0.25)\sqrt{2}}{8} \frac{\sqrt{c\sigma_z}}{h\sqrt{\sigma}}. \tag{25}$$

Note that the optimum taper angle does not depend on either the beam energy or the desired collimation depth. For the typical NLC bunch lengths and half-width h approximately 5 mm, the optimal taper angle is 5.3 mrad for copper, 12.1 mrad for titanium, 6.6 mrad for beryllium, and 28 mrad for carbon. At this taper angle the geometric and resistive contributions are equal, and the deflection (neglecting surface roughness) is given by:

$$y'_{G+R} = \frac{\sqrt{\pi} N r_e}{\gamma} \frac{h\theta_{\rm opt}}{\sigma_z} \frac{1}{r_1^2} y_0. \tag{26}$$

Similarly, for a round collimator the optimal taper angle is given by:

$$\theta_{\rm opt}^2 = \frac{\Gamma(0.25)}{\pi\sqrt{2}}\sqrt{\frac{c\sigma_z}{\sigma}}\frac{1}{r_1}, \tag{27}$$

which indicates that the optimum taper angle for a round collimator with a 1 mm aperture radius is 13.9 mrad for copper, 31.7 mrad for titanium, 17.3 mrad for beryllium, and 73 mrad for carbon. The near-center kick for a round tapered collimator with optimal taper angle is thus:

$$y'_{G+R} = \frac{2}{\sqrt{\pi}}\frac{Nr_e}{\gamma}\frac{\theta_{\rm opt}}{\sigma_z r_1}y_0. \tag{28}$$

In subsequent analyses we assume that the taper angle is equal to the optimal for all collimators. We note, however, that this optimum is a broad one: the deflection as a function of taper angle is given by:

$$y' = \frac{y'_{\rm opt}}{2}\left(\frac{\theta_T}{\theta_{\rm opt}} + \frac{\theta_{\rm opt}}{\theta_T}\right). \tag{29}$$

Thus, if the taper angle is twice the optimum the kick is only increased by 25%.

2.6.3 Jitter Amplification Figure of Merit

In the near-center regime, the question of greatest interest is how severely the collimator wakefields degrade the beam quality. Consider a collimator at a location where the beam position jitter is n times the beam size, and which results in a jitter of m times the angular divergence from wakefields. The ratio of m/n constitutes a measure of the severity of the wakefield impact on the beam quality, and permits direct calculation of the jitter amplification from the collimators given knowledge of the incoming jitter distributions. We denote the ratio m/n with the symbol $\mathcal{J}$.

Betatron Collimation Spoilers: Let us define the collimation depth of the spoilers in the betatron system to be $\pm p$ times the beam size. The jitter amplification figure is in this case given by:

$$\mathcal{J}_{\beta,sp} = r_e h\theta_T\sqrt{\pi}\frac{N}{\sigma_z}\frac{1}{p^2}\frac{1}{\gamma\epsilon}. \tag{30}$$

Interestingly, the jitter amplification does not depend upon the beam energy or the betatron function at the location of the collimators, but only upon the bunch charge/length ratio, the collimation depth, and the normalized emittance.

Betatron Collimation Absorbers: In this case, since the absorbers have fixed apertures, we eliminate use of p and instead use the betatron function at the collimator and its aperture:

$$\mathcal{J}_{\beta,ab} = \frac{Nr_e}{\gamma\sigma_z}\left(\frac{2}{\sqrt{\pi}}\frac{\theta_T}{r_1} + \frac{L_{\rm flat}\theta_{\rm opt}^2}{r_1^2}\right)\beta, \tag{31}$$

where $L_{\rm flat}$ is the flat length of the absorber between the tapers, and we have replaced a multitude of nasty variables in the flat-length expression with the optimal taper angle calculated previously. Note that the absorber jitter amplification factor depends on energy and betatron function but not on the emittance. This expression is also the correct one to use for round-aperture protection collimators. Note that Equation 31 indicates that the jitter amplification of round protection collimators is very small: a copper collimator with 20 X_0 flat section at a point with 1 km betatron functions and a minimum gap of 6 mm at 46 GeV beam energy results in a $\mathcal{J}_{\beta,ab}$ of 0.003.

Energy Collimation Spoilers: The jitter amplification figure of merit for this element is complicated because there are actually 2 such figures: one which describes the jitter amplification of

pure-betatron jitter (similar to the betatron system spoilers), and one which describes the coupling of energy jitter into betatron jitter.

The pure-betatron jitter amplification can be expressed using Equation 30. Since the spoiler gap is set according to an energy width rather than a number of beam sigmas, we can rewrite Equation 30 thus:

$$\mathcal{J}_{\beta,\delta sp} = r_e h \theta_T \sqrt{\pi} \frac{N}{\gamma \sigma_z} \frac{\beta}{(\eta \delta_{\mathrm{Max}})^2}, \tag{32}$$

where η is the dispersion function at the spoiler and δ_{Max} is the energy half-width of the aperture. The figure of merit for coupling of energy jitter to angle jitter (in radians per energy fraction) is:

$$\mathcal{J}_{\delta,\delta sp} = \frac{r_e h \theta_T \sqrt{\pi}}{\sigma_z} \frac{N}{\sqrt{\gamma}} \frac{\sqrt{\beta}}{\eta} \frac{1}{\delta_{\mathrm{Max}}^2 \sqrt{\gamma \epsilon}}. \tag{33}$$

Energy Collimation Absorbers: these are similar to the energy collimation spoilers in that they both amplify betatron jitter and couple energy jitter into the horizontal plane.

We can express the pure-betatron jitter amplification figure as:

$$\mathcal{J}_{\beta,\delta ab} = \mathcal{J}_{\beta,\delta sp} \left(1 + \frac{L_{\mathrm{flat}} \theta_{\mathrm{opt}}^2}{2 \theta_T \eta \delta_{\mathrm{Max}}} \right). \tag{34}$$

Similarly, the energy-to-angle jitter coupling figure is given by:

$$\mathcal{J}_{\delta,\delta ab} = \mathcal{J}_{\delta,\delta sp} \left(1 + \frac{L_{\mathrm{flat}} \theta_{\mathrm{opt}}^2}{2 \theta_T \eta \delta_{\mathrm{Max}}} \right). \tag{35}$$

2.6.4 Applications of Jitter Amplification Figure of Merit

The principal advantage of the jitter amplification figure of merit is that it simplifies the calculation of jitter amplification for a full system and the comparison of that amplification to a jitter budget.

Consider the betatron collimation system, in which we assume that the incoming jitter is n sigmas, in position and angle. In a given subsection of the betatron system, where the betatron phase is nearly constant because of the large beta functions, the number of sigmas of angle jitter introduced by the collimator wakefields is therefore $n \sum \mathcal{J}$, where the sum is over all collimators in the subsection. The collimator subsection in the opposite phase will have the same effect. In short, therefore, if the jitter in position and angle is n sigmas at the entrance, then the number of sigmas of jitter at the exit will be $n\sqrt{1 + (\mathcal{J}_{\mathrm{sys}})^2}$. The value of $\mathcal{J}_{\mathrm{sys}}$ can be computed from the individual $\mathcal{J}$ values according to the following rules:

- In the vertical plane, $\mathcal{J}_{\mathrm{sys}} = 2(\mathcal{J}_{\beta,sp} + \mathcal{J}_{\beta,ab})$, where the factor of 2 accounts for two iterations of collimation
- In the horizontal plane, the rule above is used except that an additional factor of $\mathcal{J}_{\beta,\delta sp} + \mathcal{J}_{\beta,\delta ab}$ must be added to account for the betatron jitter amplification due to the collimators in the energy collimation system
- In principle the horizontal jitter above must be added in quadrature with the energy-to-angle jitter coupling contribution; however, in practice the energy-to-angle jitter coupling is so small, due to the jitter cancellation principle, that this is negligible.

Another application of the amplification figure is the determination of emittance dilution. As mentioned above, the RMS kick to the beam from the dipole wakefield is 40% of the mean kick. For an RMS beam jitter of n sigmas, therefore, The emittance dilution is given by:

$$\frac{\Delta\epsilon}{\epsilon} = (0.4n\mathcal{J}_{\rm sys})^2 \,. \tag{36}$$

According to the NLC jitter budget in Table 1 the beam jitter is 0.17 sigmas (horizontal) by 0.44 sigmas (vertical) at the end of the linac. At the end of the beam delivery system the total permitted jitter is 0.2 sigmas (horizontal) by 0.50 sigmas (vertical). If we are to budget the entire BDS jitter to the betatron collimation system, then we find that $\mathcal{J}_{x,\rm sys}$ cannot exceed 0.58 and $\mathcal{J}_{y,\rm sys}$ cannot exceed 0.54. If these tolerances are met, then the emittance dilution from the near-center dipole wakefields will be less than 0.2% in the horizontal and less than 1% in the vertical.

3 New Collimation System: Overview and Beam Dynamics

As mentioned in Section 1, the collimation system consists of an energy collimation region, a betatron collimation region, and a post-collimation "dogleg" for cleanup of off-energy particles and low-energy secondaries. We describe each of these in turn.

3.1 Energy Collimation

The primary purpose of the energy collimation region is to remove particles which are too different in energy from the nominal to be properly transported in the final focus. In addition, the energy collimation system must provide energy diagnostics for the linac, protect the final focus from bunch trains which are off-energy due to klystron faults in the linac, and be capable of surviving an encounter with an off-energy bunch train. Finally, the design of the energy collimation system is not permitted to constrain the ultimate energy reach of the NLC; in practice, this means that beamlines in the beam delivery system may not use an "arc" bending geometry, but must use either "dogleg" or "chicane" geometries which allow all magnets to fit in a straight tunnel. In this way, future upgrades may be accomodated by "pushing back" and stealing real estate from the downstream end of the main linac tunnel.

3.1.1 Optical Design

Figure 10 shows the optical paramters of the energy collimation system. Collimation is provided by an adjustable-gap absorber set at the $\eta_{\rm max}$ point, which is protected by an adjustable-gap spoiler approximately 30 meters upstream of the absorber. The spoiler is protected, in turn, by a combination of a large horizontal dispersion ($\eta_{\rm spoiler} = 12$ cm) and a large vertical betatron function ($\beta_{\rm spoiler} = 14.1$ km). The parameters shown are for 1 TeV CM, at which the geometric emittances are the smallest. At lower energies, with larger geometric emittances, the vertical betatron functions may be relaxed by tuning the quadrupoles in the upstream and downstream matching regions. We have not taken credit for the potential rescaling of the vertical betatron functions in this Note, preferring to use the Z mass with the design as presented to quantify (where applicable) the worst-case dilutions of the system.

In order to achieve a "dogleg" geometry in the energy collimator, the system contains two identical collimation modules with opposite bending angles (hence oppositely-signed dispersion rays); these modules are based on FODO cells in which the drift spaces have been filled with bend magnets. In order to constrain emittance dilution from synchrotron radiation, the horizontal

betatron functions are detuned from the natural values of the FODO lattice; at 1 TeV CM, the normalized emittance growth from synchrotron radiation is 9.4×10^{-8} m.rad, or about 3.1% of the damping ring extraction emittance. The energy collimation modules are separated by a $-I$ which is needed to preserve some optical symmetries required for aberration cancellation. In addition, as we shall see, these symmetries permit a partial cancellation of the wakefields of the collimators. The horizontal width of the collimation system "footprint" is 80 cm, which can easily be accommodated by a straight tunnel layout.

In order to accept beams with a large energy error, it is necessary to use a large-aperture vacuum chamber in the dispersive regions of the system; such a design is also advantageous for pumping reasons in all parts of the design. The dispersive modules of the energy collimator assume a vacuum chamber OD of 5.08 cm, which means that the system can accomodate 10% off-energy bunch trains without risk to the vacuum system. All of the magnets in the dispersive regions are sized thus with the exception of the octupole magnets (see Section 3.4.2, below); the octupoles have a 3.0 cm full bore, but these magnets are placed at locations where the dispersion is only 4.9 cm and thus they are not at risk. The $-I$ between collimation modules also uses magnets with a 3.0 cm full bore.

Energy diagnostics are provided at the first QD in the upstream dispersive module, which is upstream of the first collimator; this location represents a trade-off between the best resolution, which is achieved at the $\eta_{\max}$ point, and suppression of backgrounds from collimation. The diagnostics include a pair of BPMs (a high-bandwidth "multibunch" BPM and a lower-bandwidth "feedback" BPM) and a laser wire scanner. The Twiss parameters at this location are: $\beta_x = 65$ meters, $\beta_y = 21.8$ km, $\eta_x = 4.9$ cm. For the largest anticipated horizontal emittance, the monochromatic beam size is 18 μm at 1 TeV CM; dividing this size by the dispersion gives an energy resolution limit from the monochromatic beam size of 370 parts per million. This limit scales as $1/\sqrt{E_{CM}}$, and is thus about a factor of 3.3 worse (1.2 parts per mil) at the Z mass.

It is anticipated that the linac will need to be commissioned and tuned before beams can be launched into the rest of the beam delivery system, and that energy diagnostics will be a necessary part of this. To accommodate this requirement, the non-dispersive $-I$ in the middle of the energy collimation system includes a kicker magnet which can be used to extract the beam downstream of the energy diagnostics but upstream of the second energy collimator. The kicker needs a rather large integrated field of 54 kG.m at 1 TeV CM, which provides a kick angle of 3.24 mrad and drives the beam out of the vacuum chamber just upstream of the first bend of the downstream dispersive module; the kick is applied in the horizontal plane. The large angle is required in order to ensure that the vacuum chamber for the kicked beam does not conflict with the next quadrupole in the energy collimator lattice. We expect this magnet will have both a DC power supply and a pulsed supply: the former will be used during linac commissioning and extensive tuning, while the latter will permit the beam to be parked downstream of the linac in the event of an MPS fault in the final focus. In the event of a failure in the kicker's pulsed power supply, the beam will impact one of the following:

- A horizontal spoiler in the betatron collimation system
- The spoiler in the second dispersive module of the energy collimator
- A sacrificial protection collimator upstream of the first QD in the second dispersive module.

3.1.2 Collimators and Wakefields

Figure 11 shows the z location of the spoiler and absorber in the upstream dispersive module. There is an additional spoiler and absorber in the matching locations in the downstream module. Both spoiler and absorber have variable-position jaws.

The absorber is 20 radiation lengths of water-cooled titanium and copper; it includes tapers to reduce wakefields and a 75 cm (20.4 X_0) flat region, as diagrammed in Figure 12. The nominal absorber full gap is 4.0 mm, which limits the energy passband to $\pm 1\%$. The spoiler is positioned 30 meters upstream of the absorber, and consists of two tapers without any flat region. The nominal spoiler full gap is set to 2.6 mm by the horizontal dispersion at that location ($\eta_x = 13.0$ cm).

Passive Survival. The RMS beam size $\sqrt{\sigma_x \sigma_y}$ required to ensure the survival of the titanium absorber is approximately 440 μm at its upstream face for 10^{12} electrons in 1 bunch train. The RMS size of the uncollimated beam at this location for the expected RMS energy spread (0.25%) and the smallest emittances (1 TeV CM, case "A") is 100 μm; the difference in quadrature between 440 μm and 100 μm must be made up by scattering from the spoiler 30 m upstream, which in turn implies a scattering angle of at least 14 μrad in each plane. Equation 11 indicates that for a 500 GeV beam, the desired scattering angle can be achieved by a 0.25 X_0 spoiler, but in the interest of additional protection for the absorber we have chosen to use a 0.5 X_0 spoiler.

The RMS beam size on the upstream face of the spoiler for the conditions stated above is 95 μm. If the 0.5 X_0 spoiler is to survive, Table 4 indicates that carbon is a suitable material, titanium alloy is marginal, and beryllium might be acceptable if the assumptions under which Table 4 was constructed are found to be overly conservative. Of the three choices, titanium alloy is the preferred material for the following reasons:

- As a metal, it has a higher conductivity and lower outgassing rate than carbon, which improves wakefield and vacuum performance, respectively
- Titanium is less expensive to machine than beryllium because beryllium flakes and dust are toxic (similarly a beryllium spoiler damaged by the beam would be considered mixed waste)
- The titanium spoiler could be shorter than beryllium, because of the short radiation length of titanium (even a spoiler made of Be would require a flat region full of material)
- Titanium is a far more common accelerator and engineering material and the community has much more experience working with titanium than either carbon or beryllium.

While the *ZDR* assumed that carbon's shortcomings were unacceptable, it is not clear that this is true in this case. The resistive-wall wakefield problem is less severe in this case than in the *ZDR* case because of wakefield cancellation. The large vacuum chamber aperture of the collimation system permits extremely high local pumping speeds near the spoiler; in addition, high-strength, low-porosity carbon ("glassy carbon") is available from a variety of industrial vendors, and this material appears to have vacuum properties comparable to metals. For the purposes of this Note, we will consider the performance of all three of these materials as spoilers, while noting that titanium remains our first choice.

While the gap sizes above are well in excess of the minimum gaps indicated in Table 3, we must also consider the possibility that the collimators will be damaged by image currents from an errant pulse which gets very close to the jaws. This is somewhat mitigated by the fact that the horizontal beam size, which is being collimated, is very large and therefore the beam begins to penetrate the collimator when the centroid is still relatively far away. We can use Equations 5 and 6 to show that in the worst case for image-current heating (which is the 1 TeV CM case "A" parameters) the image-current heating saturates when the beam centroid is 53 μ from the spoiler jaws and 283 μ from the absorber jaws. Based on the values in the last column of Table 3, this means that the heating saturates before it reaches the multi-bunch, single-train damage threshold for the absorber; thus the absorber is safe. The spoiler is also safe for beryllium or titanium alloy, but may be in danger if carbon is used, depending the particular properties of the form selected.

Near-Center Wakefields. Because the η/β ratio at the spoilers and absorbers in the energy collimation section is so large, the principal effect of these collimators is to couple energy jitter into betatron jitter, rather than to cause betatron jitter amplification. Table 5 shows the various $\mathcal{J}$ values for the spoiler and absorber in the energy collimation section for the parameters which maximize the effect of near-center wakefields (in this case, case "A" parameters at the Z peak).

Table 5: Jitter amplification figures of merit for energy collimation spoilers and absorbers; $\mathcal{J}_\beta$ is the betatron jitter amplification figure, while $\mathcal{J}_\delta$ is the coupling from energy jitter to betatron jitter, in sigmas per energy fraction. All calculations performed assuming optimal taper angle, 46 GeV per beam, case "A" parameters.

Collimator	$\mathcal{J}_\beta$	$\mathcal{J}_\delta$
Be Spoiler	0.0237	29.0
C Spoiler	0.101	123
Ti Spoiler	0.0434	53.1
Ti Absorber	0.0417	166
Cu Absorber	0.0183	33.9

Table 5 indicates that, as expected, the energy collimation system amplification of pure betatron jitter is generally quite acceptable, although at the Z-peak the amplification from carbon spoilers is uncomfortably large (note that this term varies as $1/E_{\rm CM}$). The coupling of jitter from the energy to horizontal degrees of freedom is quite large, however: in some cases, 1% energy jitter translates to over 1 sigma of transverse jitter, and this effect only improves as $1/\sqrt{E_{\rm CM}}$.

Fortunately we are able to exploit the symmetries of the collimation system to reduce the impact of the energy collimators on the beam jitter. Figure 13 shows the principle: two collimators with identical apertures are separated by a $+I$ transformation in betatron space, and posess equal and opposite dispersion functions. An off-energy beam receives a kick of $\Delta x' = \eta_s \delta \mathcal{J}_{\delta,S} \sigma_{x',S}$; this angle is transported to the matching collimator with the same sign (due to the $+I$ transform) but the offset in this collimator is reversed (due to the change in sign of the dispersion). Thus the second collimator produces a kick which cancels the kick of the first collimator. This is analogous to the cancellation of geometric sextupole aberrations in a chromatic correction section, and it is limited by the same phenomenon: the spoilers and the absorbers provide interleaved kicks which interfere with one another and cause a breakdown in cancellation.

How effective is the jitter cancellation? Figure 14 shows the horizontal offset (in sigmas) as a function of energy offset, for case "A" parameters at the Z-peak. At 1% off-energy, the remaining jitter is 13% of sigma for the baseline design (titanium spoilers and absorbers), or 27% for a system with carbon spoilers and titanium absorbers. Table 5 indicates that the carbon spoilers should each generate 1.2 sigmas of offset for 1% energy offset. The design energy jitter of the NLC is 0.22%; Figure 14 indicates that this would translate into a position jitter of 0.5% to 1.1% of sigma in this worst-case. As mentioned before, the coupling of jitter from energy to betatron phase by the collimators is expected to be inversely proportional to the square root of the beam energy.

Near-Wall Wakefields. The near-wall wakefields pose a particularly interesting machine-protection challenge to the spoiler-absorber arrangement, because a beam which passes *near* a spoiler's jaw can be deflected such that it *hits* the downstream absorber without first being spoiled. This means that the absorber must be recessed relative to the spoiler (ie, the two jaws are not perfectly "in line" with one another as seen by the beam). Numerical analyses indicate that this is a small effect, and that for a titanium spoiler the absorber should be recessed by approximately

100 μ.

Analysis of this situation is complicated by the very large energy spread of the beam: as shown in Figure 15, the beam's energy distribution is twin-horned, with an approximate full-width of 0.4%. A beam with a central energy error of 0.6% will therefore pass through the energy collimators without scraping any particles out of the core, but a larger offset will generate scraping. A partial study of the near-wall wakefields indicates that energy offsets of up to 0.9% for Z-peak running or 0.85% for 1 TeV CM produce centroid deflections which are smaller than the betatron collimation aperture; these bunch trains will safely pass through the collimation system and IP, although there will be a very large amount of backgrounds generated by tremedous particle losses (up to 75% of the train in the energy collimator alone). For all CM energies, an energy error of 1% will cause all of the primary beam particles to hit one of the two energy spoilers, which is an inherently safe situation. For centroid energy errors between 0.85% and 1%, there is a possibility that the beam will exit the energy collimation system with a sufficiently large betatron oscillation due to wakefields that it hits a betatron collimator. In this case the bunch charge will be low, and simulations to date are not sufficiently complete to indicate whether the charge density will exceed the damage threshold for the downstream spoilers.

Quadrupole Wakefields The quadrupole wakefield of the energy spoiler is assumed to be dominated by the geometric term, while the quadrupole wakefield of the absorber is assumed to be dominated by the resistive-wall contribution of its long flat section. The spoiler wakefield has a focal length of 50 km for the worst-case Z-peak parameters, comparable to 0.1% of the nearby magnetic quadrupole strengths. The absorber wakefield has a focal length of 31 km for a copper-coated titanium absorber. While these are small compared to the quad strengths, the vertical betatron functions are large. If we assume that the charge-weighted RMS quad strength is 40% of the average quad strength from these collimators, then the RMS emittance dilution due to quadrupole wakefields which vary along the length of the bunch is 15% for the worst-case Z-peak parameters. This dilution scales inversely with energy: at 1 TeV, it is reduced to 1.5%.

3.2 Betatron Collimation

The betatron collimation system is designed to remove particles which have an unacceptable amplitude in (x, x') or (y, y') phase space, and to protect the interaction region and detector from bunch trains which emerge from the linac or energy collimation system with an excessively large betatron oscillation.

3.2.1 Optical Design

The optics of the betatron collimation system is based on a symmetric FDF-polarity triplet, with an additional family of D quads near the betatron waists; the optics of the system are shown in Figure 16. The lattice provides horizontal and vertical phase advances of 90° and 270°, respectively. A total of 4.5 such cells permits two collimations in each plane and each betatron phase. As described previously, the collimators cut an inscribed rectangle in phase space, with the "corner" of the rectangle matched to the maximum amplitude the detector will tolerate for SR backgrounds. The maximum horizontal betatron function is 270 meters at the triplet F quads, which are used for horizontal collimation, while the maximum vertical betatron function is 500 meters at the triplet D quads, which are used for vertical collimation.

The magnets in the betatron collimation section, as well as the upstream and downstream matching regions, all have a bore diameter of 2 cm to permit ultra-high vacuum conditions to be achieved with reasonable pumps and vacuum chamber preparation. All magnets that are not

protected by a spoiler or absorber (see next Section) are protected by a fixed round-aperture collimator to minimize their radiation damage. We have selected a 1.2 cm full bore as a reasonable compromise between wakefields, vacuum, alignment, and protection criteria, although this may not represent a precise optimum (indeed, a precise optimum may not exist).

3.2.2 Collimators and Wakefields

The betatron collimation system contains four sets of spoilers and four sets of absorbers. The spoilers are placed next to the first and second quads of triplets 1 through 4, while the absorbers are placed next to the second and third quads of triplets 2 through 4 and the first and second quads of triplet 5 (the ".5" of 4.5 cells). This ensures that all absorbers except the last set are protected by nearby spoilers, such that even near-wall wakefields from a near-miss of one spoiler will not cause an unspoiled beam to hit the next-phase absorber.

The spoilers are tapered, adjustable jaws with an approximately rectangular gap. The present design calls for "consumable" spoilers, as shown in Figure 18: each spoiler is a disc of copper, 0.5 – 1.0 RL in thickness, with a tapered copper "wheel" surface supported by beryllium. The complete spoiler mechanism contains two such spoiling wheels; the distance between these wheels can be adjusted to vary the gap of the collimators. The beam size at the collimators is too small to ensure their survival if impacted by a high-intensity electron bunch train. Recent experiments with copper coupons indicate that under these circumstances, damage will typically be confined to a region which is a few times the beam size, and that no extensive cracks will appear [18]. Hence, in the present design, after a damage event the two wheels will rotate by approximately 6 mrad, which will present a fresh surface to the beam and move the damage spot to the side by 1 mm. In this model, each spoiler may be damaged up to 1000 times by betatron incidents. Per the discussion in Section 2.1.1, the tightest setting of the spoiler gaps occurs when operating at 500 GeV to 1 TeV CM. For Case "C" parameters at 500 GeV CM, the horizontal and vertical gaps are set to 4.8 and 17.7 σ, respectively, which corresponds to approximate half-gaps of 230 μ and 170 μ, respectively; for Case "A" parameters at 500 GeV CM, the horizontal and vertical gaps are set to 5.2 and 21.4 σ, respectively, which corresponds to approximate half-gaps of 230 μ and 160 μ, respectively. The physical gap in the vertical is smaller under Case "A" parameters than Case "C" because of the much-smaller vertical emittance in the former case. The physical gap size (in microns) is a constant from 500 GeV CM to 1 TeV CM, and increases with $1/\sqrt{E_{CM}}$ for lower energies. This means that the collimation amplitude in sigmas is constant for energies up to 500 GeV CM, and increases for higher energies, under the assumptions spelled out in Section 2.1.1.

The physical half-gaps listed above are consistent with most of the materials listed in Table 3, and copper-coated beryllium, the baseline design, is clearly viable from the point of view of fatigue damage due to image-current heating. Analysis of near-wall image-current heating indicates that the heating from a single bunch train is saturated at a distance of approximately 21 μ for both the horizontal and vertical spoiler under worst-case conditions (1 TeV CM, Case "A" emittances), while single-pulse image-current damage may occur for distances smaller than approximately 30 μ. Thus, the spoilers are potentially in danger of being damaged from image-current heating if a bunch train has a near-miss with one of the jaws.

Each set of spoilers is matched with a pair of absorbers which are placed in the next module of the collimation section. This arrangement maximizes the R_{12} and R_{34} elements from spoiler to absorber, which in turn maximizes the size of the spoiled beam on the absorber. Assuming the spoilers are 0.5 RL in thickness, the RMS horizontal and vertical divergences are 19 μrad at the downstream face of the spoiler for 500 GeV beams, which translates to approximate $\sigma_{x,y}$ values of 5.1 mm by 1.5 mm at the absorbers matched to the horizontal spoilers, and 2.1 mm by 9.2 mm at

the absorbers which are matched to the vertical spoilers. Such large beam sizes indicate that the absorbers can sensibly be made out of virtually any material listed in Table 4. In addition, since the beam sizes at the absorbers are so large, they can be made with a large fixed aperture rather than a small adjustable aperture. For this reason we presently envision cylindrically symmetric absorbers with a 2 mm full aperture. Because the gaps are so large and the only way for a beam to approach the absorbers is through a spoiler (which enlarges the beam size so dramatically), we do not consider near-wall image-current heating a problem for the absorbers.

Near-Center Wakefields: Equation 30 indicates that the jitter amplification of tapered collimators with rectangular apertures is a function of N, σ_z, $\gamma\epsilon$, and the collimation depth in sigmas. Since the collimation depth in sigmas is tightest for 500 GeV CM, this is the worst-case condition for this parameter. For both horizontal and vertical, Case "A" parameters are worse than either "B" or "C". For 500 GeV CM, Case "A" parameters, the jitter amplification figure of merit $\mathcal{J}$ is approximately 0.105 for the horizontal and 0.425 for the vertical. Note that the latter is approximately 50% larger than the maximum $\mathcal{J}$ value permitted under the arguments of Section 2.6.4. Thus, the jitter tolerances for the beam delivery system are not achievable if the analytic model for the wakefields of the collimators is correct.

Equation 31 indicates that Z-peak running with Case "A" parameters will produce the most severe jitter amplification from the absorbers. Assuming that copper absorbers are used, the amplification from the absorbers at high β_x points will be 5.8×10^{-3} (horizontal) by 2.1×10^{-3} (vertical), while the amplification from the absorbers at high β_y points will be 2.4×10^{-3} (horizontal) by 1.1×10^{-2} (vertical). As indicated in Equation 31, the jitter amplification for the absorbers scales inversely with the beam energy, therefore the absorbers are only significant sources of jitter amplification at the lowest energies anticipated. Since the jitter amplification is also inversely proportional to the aperture radius to various powers (linear for tapers, approximately cubic for untapered collimators), we neglect the contribution from protection collimators entirely.

Near-Wall Wakefields: Because the absorbers are all protected by spoilers, it is assumed that any beam which has a large enough amplitude to encounter the near-wall wakefield of the absorbers has passed through one or more spoilers and will, to good approximation, not exit the collimation system. Thus, the only relevant near-wall wakefield issue is the spoilers. Table 6 shows the maximum near-wall kick, normalized to the RMS divergence at the spoiler, for horizontal and vertical spoilers under various combinations of beam energies and parameter sets.

Table 6: Maximum spoiler kick, in units of RMS angular divergence.

E_{CM}	91 GeV		500 GeV		1 TeV	
Parameters	"A"	"C"	"A"	"C"	"A"	"C"
x Spoiler	1.58	1.34	1.87	1.59	2.12	1.82
y Spoiler	102	67	151	101	188	125

The kicks from the horizontal spoilers are relatively easy to manage in that they are comparable to the angular divergence and smaller than the aperture defined by the collimators. Assuming that a beam enters the collimator with the maximum amplitude that the collimation system will transmit (approximately 7 σ in each phase), and that each collimator contributes the maximum kick from Table 6, then the total amplitude will increase to approximately 11 σ in each plane, or a total of 15.5 σ. Assuming that the beam delivery system is designed with at least this much stay-clear under all conditions, the beam which which receives a maximum near-wall kick from the spoilers will still pass through the IP to the main dump. The only possible exception to this is the last set

of collimators in the final focus, which probably cannot meet the 15.5 σ condition outlined above.

The vertical near-wall kick is much harder to manage, since it is an order of magnitude larger than the aperture defined by the collimators. It should be noted, however, that such a large kick from one of the upstream spoilers will drive the beam into the next-phase spoilers and thus protect the final focus and detector. The only possible sequence of events which could thwart this protection is that the beam passes safely through the first 3 sets of spoilers but is within a few sigma of a jaw in the last vertical spoiler; in this case, a destructive betatron oscillation could be launched into an unprotected final focus. Such a situation can occur if there is a serious failure within the betatron collimation system itself, or potentially in the event of a rather improbable, "jackpot" combination of errors in the linac.

Quadrupole Wakefields: The worst-case quadrupole wakefields occur at the lowest energy, specifically the Z-peak running. At this energy the emittance dilution from the spoilers in a single cell is 0.3% in the horizontal and 3% in the vertical. However, the emittance dilution from the quadrupole wakes in the first cell is nearly cancelled by the wakefields in the third cell due to the $-I$ between these cells; the second and fourth cells execute a similar cancellation. Thus the emittance dilution from quadrupole wakefields is negligible for all operating conditions of the betatron collimation system.

3.3 Post-Collimator Dogleg

The beampipe immediately downstream of the betatron collimation section is expected to contain low energy debris from the collimation process: simulations of collimation indicate that the spectrum of transmitted particles can be as much as 16% below the nominal energy. In order to further reduce the number of particles which reach the final focus, the betatron collimation system is followed by a dispersive region in which off-energy particles can be removed. In order to obey the guidelines on energy expandability of the beam delivery system, the post-collimation cleanup is arranged in a short dogleg with opposite bending polarities from the energy collimation system.

3.3.1 Optical Design

Figure 17 shows the optical functions of the post-linac dogleg. The basic optical module is a 90° by 90° FODO lattice of combined function bending and focusing magnets, with $\beta_{\max}$ of 31.3 m, $\beta_{\min}$ of 6.8 m, and $\eta_{\max}$ of 1.26 cm. The sign of the matched dispersion function is flipped in the middle of the dogleg; this is accomplished by a pair of cells which are matched to the arc cells but contain no bending elements, in essence forming a non-dispersive $-I$ module. In addition, a single cell with no bending precedes the first arc cell, which optimizes the phase advance between the energy collimation and dogleg regions for control of high-order dispersion. In order to accomodate dispersion-matching cells, arc cells, and nonbending cells, the dogleg magnets are envisioned as pure quadrupole magnets which are offset in x to achieve their bending where bending is required. The required offsets are typically mm-sized, with a 3.45 mm offset required in the dispersion suppressor and matcher. The quads are assumed to have a full aperture of 2 cm, so such offsets are not unreasonable. The dogleg also contains 8 sextupoles in 4 families for additional aberration control, although in the present deck they are set to zero.

The emittance dilution of the system is quite small despite its large dispersion functions: 2% at 1 TeV CM. The expected energy aperture is approximately 8%, assuming that the absorbers used in the dogleg are identical to the ones used in the betatron collimation system (ie, 2 mm full aperture).

3.4 Global Issues

3.4.1 Summary of Near-Center Wakefield Effects and Budgets

Table 7, below, summarizes the jitter amplification due to collimators in the NLC post-linac collimation system, assuming that the baseline design (Ti spoilers and Cu-coated Ti absorbers in the energy collimation system, Cu spoilers and absorbers in the betatron collimation system) is used. As mentioned previously, the jitter amplification in the vertical is quite large and constitutes a potentially severe limitation. We have not tabulated emittance dilution due to near-center wakefields since even in the worst case the vertical emittance dilution is only 3.3%.

Table 7: Jitter amplification figures for NLC post-linac collimation system. X and Y depth are collimation depths in sigmas. $\mathcal{J}_{\delta,\mathrm{sys}}$ refers to the energy-to-betatron jitter of the full energy collimation system assuming approximately 0.25% energy jitter (as the coupling factor is nonlinear), and has dimensions of beam sigma per energy fraction. Values of $n\sigma_{\mathrm{jit}}$ are jitter amplitudes, in sigmas, at end of collimation system assuming that incoming jitters are as in Table 1.

	91 GeV CM			500 GeV CM			1 TeV CM		
	A	B	C	A	B	C	A	B	C
$\mathcal{J}_{\beta,\delta\mathrm{sp}}$	0.0439	0.0386	0.0403	0.0080	0.0070	0.0073	0.0040	0.0035	0.0037
$\mathcal{J}_{\beta,\delta\mathrm{ab}}$	0.0367	0.0322	0.0337	0.0067	0.0059	0.0061	0.0034	0.0030	0.0030
$\mathcal{J}_{\delta,\mathrm{sys}}$	3.20	2.65	2.67	1.37	1.13	1.14	0.97	0.80	0.81
X Depth	5.2	4.8	4.8	5.2	4.8	4.8	7.5	6.8	6.8
Y Depth	21.4	18.6	17.7	21.4	18.6	17.7	30.7	29.5	25.3
$\mathcal{J}_{x,\mathrm{sp}}$	0.105	0.096	0.094	0.105	0.096	0.094	0.051	0.048	0.047
$\mathcal{J}_{x,\mathrm{ab}}$	0.049	0.043	0.045	0.0089	0.0078	0.0082	0.0045	0.0039	0.0041
$\mathcal{J}_{y,\mathrm{sp}}$	0.425	0.361	0.312	0.425	0.361	0.312	0.207	0.143	0.153
$\mathcal{J}_{y,\mathrm{ab}}$	0.090	0.079	0.083	0.016	0.014	0.015	0.008	0.007	0.008
$\mathcal{J}_{x,\mathrm{sys}}$	0.389	0.349	0.352	0.243	0.221	0.217	0.118	0.111	0.109
$\mathcal{J}_{y,\mathrm{sys}}$	1.030	0.880	0.790	0.882	0.750	0.654	0.430	0.300	0.322
$n\sigma_{x,\mathrm{jit}}$	0.182	0.180	0.180	0.175	0.174	0.174	0.171	0.171	0.171
$n\sigma_{x,\mathrm{jit}}$	0.632	0.586	0.561	0.587	0.550	0.526	0.479	0.459	0.462

3.4.2 Magnet Specifications

The energy collimation system and the linac-to-ecoll matching region use a total of three families of quads: the main linac long quad (97.8 cm long, 1.27 cm full bore); a large-bore quad for dispersive regions (100 cm long, 5.08 cm full bore); and a smaller-bore quad for the $-I$ between modules (100 cm long, 3 cm full bore).

The energy collimation system uses a single family of DC bend magnets, which is presently modelled as having an effective length of 4.52 meters. While this is inconveniently long, it is necessary to maximize the packing fraction of bend magnets in the system to minimize synchrotron radiation growth. The single beam dumper magnet is based on the SLAC damping ring complex pulsed bend magnet PBH, which is designed to pulse at up to 10 kG peak field with 120 Hz repetition rate [39]. A duplicate of this magnet is used to dump the SLAC linac beams at the end of sector 2, and has actually operated for significant periods of time at 120 Hz [39].

Table 8: Specification of quadrupoles in energy collimation section and matching section from main linac to energy collimation. Field strengths are specified at 1 TeV CM, count is for one side of one IR only.

Name	Count	$\int G.dl$, kG	Full bore, cm	Length, cm	B_0, kG
QF3EC	2	493.1	1.27	97.8	3.202
QF2EC	2	1018	1.27	97.8	6.118
QD1EC	3	1241	1.27	97.8	8.058
QF1EC	2	1058	1.27	97.8	6.872
QFEC	8	186.4	5.08	100	4.735
QDEC	8	186.4	5.08	100	4.735
QFMI	4	550.3	3.00	100	8.254
QDMI	4	550.3	3.00	100	8.254

Table 9: Specification of bend magnets in energy collimation. Field strengths are specified at 1 TeV CM, count is for one side of one IR only.

Name	Count	$\int B.dl$, kG.m	Full bore, cm	Length, cm	B_0, kG
B1	12	2.02	5.08	452	0.446
B2	12	0.45	5.08	452	0.099
B3	12	2.02	5.08	452	0.446
B4	12	0.45	5.08	452	0.099
SBD	2	27.0	3.00	300	9.000

In addition to quads, DC bends, and pulsed bends, the energy collimation system uses a family of sextupoles (5.08 cm full aperture, 1 m length) and a family of octupoles (3.0 cm full aperture, 1 m length).

Table 10: Specification of sextupole and octupole magnets in energy collimation. Field strengths are specified at 1 TeV CM, count is for one side of one IR only.

Name	Count	Full bore, cm	Length, cm	B_0, kG
SXEC1	2	5.08	100	0.454
SXEC2	2	5.08	100	0.454
SYEC1	4	5.08	100	1.600
SYEC2	4	5.08	100	1.600
OCTEC1	1	3.00	100	5.402
OCTEC2	1	3.00	100	4.836
OCTEC3	1	3.00	100	5.402
OCTEC4	1	3.00	100	4.836

All quads in the match from energy to betatron collimation, and the betatron collimation system itself, are one family: full aperture of 2.0 cm, length of 2.0 meters.

Table 11: Specification of quadrupoles in betatron collimation section and matching section from energy to betatron collimation. Field strengths are specified at 1 TeV CM, count is for one side of one IR only.

Name	Count	$\int G.dl$, kG	Full bore, cm	Length, cm	B_0, kG
QF1BC	2	1219	2.0	200	6.100
QD1BC	4	889.1	2.0	200	4.446
QF2BC	2	873.0	2.0	200	4.365
QFBCOL	9	735.4	2.0	200	3.677
QDBCOL	4	1132	2.0	200	5.661
QCBCOL	9	1012	2.0	200	5.059

All of the separated-function quadrupoles in the dogleg and the match from the betatron collimator to the dogleg are in the same family as the betatron collimation quads.

Table 12: Specification of quadrupoles in dogleg section and matching section from betatron collimation to dogleg. Field strengths are specified at 1 TeV CM, count is for one side of one IR only.

Name	Count	$\int G.dl$, kG	Full bore, cm	Length, cm	B_0, kG
QDDB1	1	772.0	2.0	200	3.860
QFDB1	1	1065	2.0	200	5.327
QDDB2	1	470.9	2.0	200	2.355
QDDB3	1	247.1	2.0	200	1.236
QFDL	12	942.8	2.0	200	4.714
QDDL	12	942.8	2.0	200	4.714

The combined-function magnets (bend/quadrupole) in the dogleg have been modelled as a pure quadrupole which is physically offset from the centerline of the accelerator to achieve the desired bending field. In actual implementation it may prove to be more optimal to use properly-aligned quads with differential pole excitation currents to achieve the bending, or to achieve the magnet parameters in some other way. In the specifications of the combined-function magnets below, we include both the desired bending field and the necessary offset to achieve the bending if the magnet is modelled as a 2 meter long, 2 cm full aperture pure quad, as the single-function dogleg quads are.

Table 13: Specification of combined-function bend/quad magnets in dogleg. Field strengths are specified at 1 TeV CM, count is for one side of one IR only.

Name	Count	$\int B_{\rm bend} dl$, kG.m	$\int G.dl$, kG	Full bore, cm	Length, cm	$B_{\rm bend}$, kG	$B_{\rm quad}$, kG	Offset, mm
BQFDL1	8	1.869	942.8	2.0	200	0.935	4.714	1.98
BQDDL1	8	2.092	942.8	2.0	200	1.046	4.714	2.22
BQFDL2	8	1.869	942.8	2.0	200	0.935	4.714	1.98
BQDDL2	8	2.092	942.8	2.0	200	1.046	4.714	2.22
BQMF1	2	3.256	942.8	2.0	200	1.628	4.714	3.45
BQMF2	2	0.755	942.8	2.0	200	0.378	4.714	0.80
BQMD	4	0.606	942.8	2.0	200	0.303	4.714	0.64
BQSF1	2	3.256	942.8	2.0	200	1.628	4.714	3.45
BQSF2	2	0.755	942.8	2.0	200	0.378	4.714	0.80
BQSD	4	0.606	942.8	2.0	200	0.303	4.714	0.64

In addition to the separated-function quads and the combined-function bend/quads, the dogleg contains several sextupole magnets which at the present time are set to zero strength and may be removed from the design. Nonetheless we include their parameters in the interest of completeness.

Table 14: Specification for sextupole magnets in post-collimation dogleg. Count is for one side of one IR only.

Name	Count	Full Bore, cm	Length, cm
SXDL1	1	2.0	50
SXDL2	1	2.0	50
SXDL3	1	2.0	50
SXDL4	1	2.0	50
SYDL1	1	2.0	50
SYDL2	1	2.0	50
SYDL3	1	2.0	50
SYDL4	1	2.0	50

3.4.3 Bandwidth and Dynamic Aperture

Two measures of the global optical performance of the collimation system are its bandwidth (the range of centroid energies over which the beam remains well-behaved), and the dynamic aperture

(more generally the 5-dimensional volume of particles which can be transported safely through the system). The former is primarily related to the luminosity limitations which arise in the collimation system, while the latter is more connected to whether the collimation system has optical properties which tend to repopulate the halo after collimation (i.e., whether the collimation system is a background source rather than a background cure).

Bandwidth: The bandwidth was studied by transporting a monochromatic, matched beam with a centroid energy offset through the collimation system and measuring the emittance, mismatch parameter, and centroid offset at the end of the collimation system. This measurement was performed with two sets of emittances: the smallest geometric emittances ($\gamma\epsilon_{x,y} = 3 \times 0.03$ mm.mrad, 1 TeV CM), and the largest geometric emittances ($\gamma\epsilon_{x,y} = 4.35 \times 0.096$ mm.mrad, at the Z-peak). For both measurements the optics was the nominal optics shown in Figure 2, and the sextupoles and octupoles were tuned to their nominal values.

Figure 19 shows the emittance dilution factor, $\epsilon_f \cdot BMAG/\epsilon_i$, as a function of centroid energy error ($BMAG$ is a measure of the mismatch of the beam, defined such that the beam size at the IP for a design β^* is given by $\sqrt{\epsilon_f \cdot BMAG\beta^*}$); the emittances are the smallest possible as defined above. The luminosity dilution is determined by the horizontal mismatch over the range of interest. If we take a 10% dilution as our figure of merit, the total bandwidth of the collimation system is approximately 3.5%. Figure 20 shows the same simulation for the largest emittances expected, as defined above. While the horizontal emittance dilution is nearly the same (indicating that the dilution is due to various orders of chromaticty, leading to a mismatch for off-energy bunches), the vertical emittance dilution is somewhat larger than in Figure 19. This indicates that the vertical emittance dilution is itself a function of the emittance, which implies the presence of chromogeometric aberrations. Nonetheless, the system performance is still acceptable, with a total bandwidth of approximately 2.7%. Furthermore, the vertical bandwidth at lower energy can be improved by reducing the vertical β functions in the energy collimation section, as the geometric emittances are much larger.

Figure 21 shows the beam centroid position in (x, x') phase space for various centroid energies from -3.2% to +3.2%. The circle in the plot is the design 1 σ phase space for the minimum emittance case; the low-energy centroid is to the right, high-energy to the left. Figure 21 indicates that there is a substantial contribution from high-order dispersion in the present design. The high-order dispersions have been minimized by careful use of symmetries to eliminate first- and second-order dispersions, by adjusting the phase advance between the energy collimation system and the dogleg, and by tuning the sextupoles in the energy collimation section, and tuning several octupoles in the energy collimation system. It is worth noting that the dispersions are high-order (i.e., the offset is proportional to energy error raised to a high power), and that even 3% off-energy centroids are acceptably close to the design orbit for the smallest geometric emittances. Therefore we expect that over the luminosity bandwidth of the system, centroid offsets from high-order dispersion will not cause significant luminosity loss.

Dynamic Aperture: A preliminary survey of the dynamic aperture of the full beam delivery system indicated that overall the linearity of the optics is reasonably well preserved for particles which are within the collimation aperture in all degrees of freedom. There were, however, a small number of particles which passed through all the collimators and still entered the "no-fly zone" in the final doublet. These particles were off-energy and also at large horizontal betatron amplitudes; no determination was made as to whether the particles were driven out by nonlinearities in the collimation system, the final focus, or a combination of both. Since that time the final focus design has evolved, and more changes appear certain. Thus, we have postponed further study of this issue, but note that the dynamic aperture does not appear to be drastically small.

3.4.4 Vacuum Requirements

The vacuum pressure requirements for the collimation section are determined by the following physics criteria:

- Avoidance of instabilities related to residual gas presence, such as the fast beam-ion instability
- Limiting halo repopulation in the collimation section.

Halo repopulation: The criterion, since the *ZDR*, is that the number of halo particles generated by elastic and inelastic beam-gas scattering should be smaller than the number of halo particles from the linac which are transmitted through the collimation system. Since the beam halo is expected to be no larger than 10^9 particles per bunch train (see Section 2.2.6), and the transmission is expected to be approximately 10^{-5} (see Section 4.1), this means that the beam-gas repopulation of the halo should not exceed 10,000 particles integrated over the entire collimation system. In a study of the *ZDR*-era beam delivery system, it was found that over the full 5 km system a base pressure of 10^{-8} torr led to scattering of a few thousand particles, of which about 1500 were scattered to sufficiently large amplitude to be lost [40]. While no comparable study has been performed for the present system, we assume that its performance will be even better than that of the full system studied in [40], for the following reasons:

- The collimation system is only 1.5 km in length, while the ZDR system was 5 km in length
- The ZDR system which had extremely large betatron functions in both its collimation system and its final focus, which are much worse from a scattering point of view because they lead to small beam divergences (thus a small angular scatter translates to a large number of sigmas); the present collimation system has much more modest betatron functions and thus is likely to be more robust against scattered particles.

Because of the factors listed above, we expect that 10^{-8} torr will be more than adequate vacuum performance. In order to achieve this, the majority of beamline components have full apertures of 2, 3, or even 5 cm to allow adequate pumping with modest numbers of ion pumps. Only the first few quads have a small, 1.27 cm full aperture, which matches the aperture of the upstream linac quads; this section of the beamline will probably use an extension of the linac beamline vacuum system.

Fast Beam-Ion Instability: At this time no studies have been performed of this phenomenon as it applies to the collimation section.

3.4.5 Proposed Locations for Feedback Loops

Feedback loops in the collimation system are likely to be difficult to implement due to interference from lost particles affecting the BPMs. Nonetheless, one can compile a "wish list" of locations where feedbacks would be desirable:

- Energy feedback for the main linac using horizontal BPMs at the first QD after the first energy collimation bend. This is presently part of the system design, and is immune to halo interference because the first collimator is downstream of this location.
- Feedback to maintain horizontal and vertical steering through the sextupoles and octupoles in the energy collimation system.
- Feedbacks to maintain the beam position in the 4 sets of betatron collimation spoilers.

3.4.6 Tolerances

It is expected that the sensitivity of the luminosity to misalignments and errors in the collimation system will be several times looser than in the *ZDR* system, due to the generally more relaxed optical functions of the new system. This is also suggested by the relatively large bandwidth of the system compared to its predecessor.

In addition to tolerances which must be met in order to preserve the luminosity, the collimation system's strong optics and small collimator apertures set moderately tight tolerances on the amount of quadrupole motion which can be tolerated due to the danger of driving the primary beam into a spoiler. Figure 22 shows the allowed horizontal motion of the quads in the collimation system from this limit; the minimum tolerance is approximately 30 micrometers. Figure 23 shows the equivalent vertical limits, which are somewhat tighter: many magnets have tolerances which are just below 5 micrometers. Such tight tolerances indicate that steering feedbacks at the collimator jaws are likely to be essential to prevent diurnal differential motions of the beamline magnets from endangering the collimator jaws. Note that the equivalent tolerances in the *ZDR* system were closer to 1 micrometer; this also suggests that other tolerances in the new collimation system are looser than the tolerances in the old system by a substantial factor.

3.4.7 Operation at High Luminosity

In addition to the standard "operating plane," there is understandable interest in the maximum luminosity achievable in the NLC. A set of parameters which would permit operation at 3–4 times the luminosity of the operating plane has been suggested [4]. The principal differences between the operating plane and high-luminosity operation are increased beam power (190 bunches per train at 0.75×10^9 particles per bunch), reduced emittances in the linac and beam delivery regions ($\gamma\epsilon_{x,y} = (360, 3.5) \times 10^{-8}$ mm.mrad at IP), and reduced values of β^* (8×0.1 mm at 500 GeV CM, 10×0.12 mm at 1 TeV CM). The RMS bunch length for these parameter sets is 110 μm. These parameters have the potential to impact the collimation system in the following ways:

- The increased beam power density may put the spoilers and absorbers in the energy collimation modules at risk of single-train damage
- The reduced emittances may cause additional jitter amplification
- The collective-damage mechansisms such as image-current heating may be worse.

At this time no emittance budgets have been established for the high-luminosity parameters. For our purposes we assume that the end-linac parameters are equal to those listed above. Note that so little emittance dilution is permitted under this scheme that the details of the allocation budget are unlikely to have much impact on the conclusions below.

The RMS beam size at the energy spoiler will be 300×32 microns for 500 GeV CM and 300×22 microns for 1 TeV CM. This gives an RMS size of 99 microns at the lower energy and 81 microns at the higher energy. The charge in 1 bunch train is 1.4×10^12 particles, therefore the safe RMS size for a 0.5 X_0 titanium alloy spoiler is 118 microns. Given the RMS divergence angles induced by the spoiler, the RMS beam size at the absorber would be 520 μm for 1 TeV CM, while the minimum safe size is also 520 μm. As mentioned previously, the safe beam size calculated for a thin spoiler from materials properties is probably somewhat conservative, but the safe beam size for an absorber is likely to be relatively accurate. We therefore conclude that both the spoiler and the absorber in the energy collimation region may still satisfy the criterion of passive survival, but our confidence in this conclusion is not high.

The IP parameters required for high-luminosity operation in turn require that the collimation depth be set to 4.2×25.3 sigmas at 500 GeV CM, and 6.8×39.3 sigmas at 1 TeV CM. These collimation depths, coupled with the bunch charge, length, and emittance, give jitter-amplification figures of 0.140×0.400 at 500 GeV CM, and 0.054×0.166 at 1 TeV CM. In both cases the horizontal amplification will be slightly worse than the "A" parameters of the operating plane, and the vertical amplification will be slightly better.

In order to achieve the collimation depths listed above, the collimator gaps must be set to 188×151 microns at 500 GeV CM, and 214×166 microns at 1 TeV CM. The single-bunch image-current heating is actually reduced from case "A", since the ratio of Q/σ_z is smaller. Because the number of bunches is doubled, the single-train image current heating is larger than for the operating plane. The half-gap that ensures the spoilers are safe from fatigue damage goes to 133 micrometers for titanium alloy, 102 micrometers for beryllium, and 89 micrometers for copper; thus the gap sizes above are safe from this point of view.

4 New Collimation System: Collimation Quality

The NLC collimation system is not worth the clock cycles it's made out of if it cannot effectively reduce the backgrounds experienced by the detectors. In order to do this, it must efficiently remove halo particles and minimize the production of muons which can be transmitted to the IP.

4.1 Collimation Efficiency

How efficiently must the collimation system reduce the beam halo prior to the final focus? An answer can be found in Figure 4, which shows the ratio of stopped electrons to IP muons as a function of the z location of the electron collimator. The rightmost point in this figure is the high-β point in the final focus at the first set of sextupoles, where typically 10,000 to 40,000 stopped electrons will generate one muon in the detector. If the halo contains 10^9 particles per bunch train, it follows that the collimation system transmission must be between 1×10^{-5} and 4×10^{-5}, with smaller numbers always preferred.

Simulation studies have indicated that transmission is maximized for halo particles which are matched to the optics of the first spoiler they encounter (i.e., their position/angle correlation is correctly modelled by the design β and α function at the spoiler), which are close to the edge of the spoiler, and for beams at the highest energy. Therefore, we use as our figure of merit the transmission of 500 GeV halo particles which are matched to the lattice and which impact the spoilers near their edges. We have not studied the efficiency of the energy collimation system, since any particle which encounters the energy spoilers will go to a large betatron amplitude and either stop at the energy absorbers or else be collimated by the betatron system, therefore its efficiency is by definition at least as good as the betatron system's.

Figure 24 shows the transmission from the first and second set of spoilers, horizontal and vertical, based on the criteria above. For this study no final collimation of off-energy particles has been performed in the dogleg, and the incident beam energy is 500 GeV. Assuming 0.5 X_0 spoilers in the betatron collimation section, the maximum transmission is 8.2×10^{-5}; assuming instead 1.0 X_0, the maximum transmission falls to 5.5×10^{-6}. Assuming that an additional set of energy cleanup collimators in the dogleg gives an additional improvement of about a factor of 4, either thickness will suffice to hit the target transmission figure of 10 to 20 parts per million.

In the present design we specify 0.5 X_0 spoilers in the betatron collimation system in order to minimize near-wall wakefield deflections and heating of the downstream face of the spoiler by electromagnetic showers from halo particles. Since the worst-case transmission is acceptable for

this design, we assume that the actual transmission averaged over mismatched halo particles and halo particles at much larger amplitudes will be quite comfortable. In the event that this proves to be untrue, we hold in reserve the possibility of using 0.7 to 1.0 X_0. spoilers.

4.2 Muon Production and Spoiling

Because of their long lifetimes, high energies, and high penetrating power, muon secondaries from the collimation system absorbers are a potentially significant source of background for the NLC's detectors, and as such have been extensively studied. The aforementioned Figure 4 shows the number of electrons which may be stopped at each absorber to produce one muon which enters the detector. The acceptable muon backgrounds in the detector are not well-determined; indeed, the actual limitation is likely to be a muon density (in particles per square centimeter), and the limit is likely to be different in the various detector subsystems. Nonetheless, a rate of zero muons per bunch train is obviously quite good, while 1000 muons per bunch train seems excessive.

The blue diamonds and black circles in Figure 4 show the electron/muon ratio for a beamline with no particular attention paid to muon backgrounds. The levels are extremely low, with 1 muon per 10^5–10^6 collimated electrons. Since this is not acceptable, we have incorporated a pair of muon spoilers into the design. These are tunnel-filling iron blocks with current windings, which produce a toroidal magnetic field to deflect muons away from the detector. The purple triangles and red squares represent the electron/muon ratio if two spoilers are used: a 9 meter long spoiler 900 meters upstream of the IP, and an 18 meter long spoiler 300 meters upstream of the IP. The performance in this case is considerably improved.

Given the results in Figure 4, how many muons can we expect per bunch train in the detector? Since the limits are obviously tighter for the betatron system, let us consider 10^9 particles incident on the first set of spoilers in the betatron system. Transmission to the third set of spoilers is about 0.2%; roughly 10% of these particles reach the fourth section. Thus, there are roughly 5×10^8 particles stopped in each of the first two absorbers, 1×10^6 particles stopped in the third absorber, and 1×10^5 stopped in the fourth absorber. From Figure 4, the number of muons per bunch train per side into the detector is therefore 1.9 for 500 GeV CM and 28.3 for 1 TeV CM. The former is clearly acceptable, but the latter may be too much. Given that this result is based on halo populations which may be pessimistic, and transmission between sections of the betatron collimation system which may be optimistic or pessimistic, our present philosophy is to declare that the results above are acceptable for most energies up to 1 TeV CM. In the event that the muon backgrounds are too high at 1 TeV CM, we expect that 1 or 2 more spoilers will reduce the backgrounds to acceptable levels.

The scaling of muon background with beam energy is somewhat unclear. The minimum muon energy required to reach the IP through the present family of magnetized spoilers is approximately 180 GeV. Conseqently the muon backgrounds can be expected to fall rapidly to zero as the beam energy is reduced to 180 GeV, and to climb in a nonlinear fashion as the energy is raised over the present 500 GeV per beam benchmark.

5 System Scaling Laws

One of the crucial questions for any part of the NLC is the equations which govern its properties as a function of energy. The most critical parameter is the length of the system as a function of energy. A brief examination of the scaling laws reveals that the relationship between length and beam energy is not a simple one: as the design energy is changed the other parameters, such as

bunch charge, are also changed, which in turn leads to further changes in the system length to meet new requirements imposed by the parameters which are "downstream" of the energy.

In the following sections, we attempt to find the equations which govern the relationships between the following parameters: beam energy (E); system length (L); bunch charge (n); bunch train charge (N); bunch length (σ_z); momentum passband (δ_M); energy spread (σ_δ); horizontal and vertical betatron functions ($\beta_{x,y}$); horizontal and vertical normalized emittances ($\gamma\epsilon_{x,y}$); horizontal dispersion function (η). In all of the following we follow the prescription of Irwin and state that all parameters are normalized to their values in the NLC design at 1 TeV CM.

5.1 Energy Collimation

The energy collimation section has six fundamental requirements which govern its parameters:

- The vertical betatron function, which is enlarged to protect the spoilers, is constrained by the limited amount of chromaticity which the system will tolerate.
- The beam size at the spoiler must be large enough to prevent its destruction by one bunch train.
- The spoiled beam size at the absorber must be large enough to prevent its destruction by one bunch train.
- In order to separate the collimation in momentum and betatron amplitude the ratio of horizontal dispersion to horizontal betatron function must be large.
- The distance from the beam centroid to the collimator jaw must be sufficient to avoid damage to the jaw from image-current heating or other collective effects.
- The synchrotron radiation emittance dilution must be constrained.

The requirements listed above can be translated to the following inequalities:

$$\frac{L}{\beta_y} \geq 1 \tag{37}$$

$$\frac{NE^{1/2}}{\eta\sigma_\delta\beta_y^{1/2}\gamma\epsilon_y^{1/2}} \leq 1 \tag{38}$$

$$\frac{NE^2}{L^2} \leq 1 \tag{39}$$

$$\frac{E^{1/2}\eta}{L^{1/2}\gamma\epsilon_x^{1/2}} \geq 1 \tag{40}$$

$$\frac{\eta\delta_M\sigma_z}{n} \geq 1 \tag{41}$$

$$\frac{E^6\eta^5}{L^5\gamma\epsilon_x} \leq 1. \tag{42}$$

In Equations 37 through 42 there are a total of 11 parameters and 6 equations. Of the 10 parameters, eight of them are set by the requirements of the linac, final focus, or detector: E, $\gamma\epsilon_x$, $\gamma\epsilon_y$, σ_z, δ_M, σ_δ, N, n; one of the inequalities, Equation 41, can be neglected because, in our judgement, any system which satisfies the other inequalities is likely to be extremely satisfactory

from the point of view of collective heating and electric fields on the collimator jaws. This leaves five inequalities and three free parameters: L, β_y, and η.

The inequality in Equation 42 represents a maximum dispersion tolerable for a given length, while the inequality in Equation 37 represents a maximum β_y tolerable for a given length. Since the inequality in Equation 38 prefers larger dispersion and betatron functions, we can combine these three inequalities into one:

$$L \geq \frac{N^{2/3}E^{17/15}}{\sigma_\delta^{2/3}\gamma\epsilon_y^{1/3}\gamma\epsilon_x^{2/15}}. \tag{43}$$

Similarly, we can use the inequalities in Equations 40 and 42 to establish an independent limit on L:

$$L \geq \gamma\epsilon_x^{3/5}E^{7/5}. \tag{44}$$

We now have 3 independent inequalities for determining the minimum system length given the fixed collider parameters, and additional equations for determining the maximum betatron and dispersion functions from the length:

$$\begin{aligned} L &= MAX\left(\gamma\epsilon_x^{3/5}E^{7/5},\ \frac{N^{2/3}E^{17/15}}{\sigma_\delta^{2/3}\gamma\epsilon_y^{1/3}\gamma\epsilon_x^{2/15}},\ EN^{1/2}\right), \\ \eta &= \frac{L\gamma\epsilon_x^{1/5}}{E^{6/5}}, \\ \beta &= L. \end{aligned} \tag{45}$$

5.2 Betatron Coll

The betatron collimation system's requirements are a subset of the requirements for the energy collimation system. Specifically, the betatron collimator must satisfy the first, third, and fifth conditions (limit chromaticity, protect absorbers, limit collective heating effects). Thus:

$$\frac{L}{\beta_{x,y}} = 1 \tag{46}$$

$$\frac{NE^2}{L^2} \leq 1 \tag{47}$$

$$\frac{p_{x,y}\gamma\epsilon_{x,y}^{1/2}\beta_{x,y}^{1/2}\sigma_z}{E^{1/2}n} \geq 1, \tag{48}$$

where we have introduced p for the collimation depth. Since β_x and β_y both scale linearly with length, we can reduce these inequalities to one expression for the system length:

$$L = MAX\left(EN^{1/2},\ \frac{En^2}{\sigma_z^2 p_x\gamma\epsilon_x},\ \frac{En^2}{\sigma_z^2 p_y\gamma\epsilon_y}\right). \tag{49}$$

5.3 Dogleg

The primary requirement on the post-collimation dogleg is that emittance dilution must be minimized. Technically, the dispersion/betatron ratio must be adequate, and one would therefore naively assume that the system scaling law should be:

$$\begin{aligned} L &= \gamma\epsilon_x^{3/5}E^{7/5}, \\ \eta &= \gamma\epsilon^{4/5}E^{1/5}. \end{aligned} \tag{50}$$

However, for the present system the dispersion/betatron ratio is extremely good and therefore we assume that the scaling may be a constant-dispersion scaling:

$$\begin{aligned} L &= E^{6/5}\gamma\epsilon_x^{-1/5}, \\ \eta &= 1. \end{aligned} \tag{51}$$

5.4 System Length for Alternate LC's

An interesting exercise is to compute the length of the collimation system for assorted linear collider designs other than the NLC, using the equations above. We consider both the TESLA superconducting collider at 800 GeV CM and the CLIC two-beam collider at 3 and 5 TeV CM.

5.4.1 TESLA at 800 GeV CM

The scale factors for TESLA IP parameters relative to NLC are as follows [41]:

- $E = 0.8$
- $n \approx 2$
- $\gamma\epsilon_x \approx 3$
- $\gamma\epsilon_y \approx 0.6$
- $\sigma_z \approx 4$
- $\sigma_\delta \approx 0.1$–$1$,

where the large spread in σ_δ is a result of the TESLA scheme to generate positrons via a wiggler at the end of the electron linac; the wiggler increases the electron beam energy spread to a level similar to NLC, while the positron side has a much smaller energy spread. The issue of N scaling is also tricky, since the TESLA bunch spacing is 337 nsec. This means that, unlike other linear colliders, the TESLA collimators need not absorb an entire bunch train, as the time between the first bunch and the last is so long that an upstream abort may be used. We have assumed that 25 bunches (8.4 microseconds) impact the spoilers and absorbers, therefore $N \approx 0.5$.

The positron collimation system has a very small energy spread; because of this, in order to achieve passive protection the energy collimation system must be 2.3 times as long as NLC's. On the electron side, where the energy spread is larger, the system still must be 1.4 times as long as NLC's to achieve the same spectrometer quality, due to the large horizontal emittance. For both systems the betatron collimation system may be 57% as long as NLC's, and the dogleg may be 61% as long.

5.4.2 CLIC at 3 TeV CM and 5 TeV CM

The scale factors for CLIC beam delivery parameters relative to the NLC, for 3 TeV CM/5 TeV CM, are as follows [42]:

- $E = 3.0/5.0$
- $n \approx 0.4/0.4$
- $N \approx 0.6/0.6$

- $\gamma\epsilon_x \approx 0.2/0.2$
- $\gamma\epsilon_y \approx 0.2/0.2$
- $\sigma_z \approx 0.3/0.25$
- $\sigma_\delta \approx 1/1.$

The scalings for CLIC are somewhat unfavorable: the energy collimation system must be 5.2 times as long as NLC's at 3 TeV CM, and 9.3 times as long at 5 TeV CM, due primarily to the very small vertical emittance which makes passive survival of the spoilers difficult; the betatron collimation system must be 5.2 times as long at 3 TeV CM and 6.4 times as long at 5 TeV CM, driven by the damage limits from image-current heating; even the dogleg must be 5.2 to 9.5 times as long at 3 and 5 TeV CM, respectively. For beams with such a high center-of-mass energy and such small emittances, it seems that another concept for the collimation system must be considered, or else that some of the requirements of the NLC system must be relaxed.

6 Conclusions and Future Directions

Because of the high beam power density and low repetition rate of the NLC, the design of the post-linac collimation system must strike a balance between halo removal, emittance dilution, and self-preservation. We have presented a system which strikes such a balance, along with some approximations which indicate the scaling of system parameters (typically, length and optical functions) as the various machine parameters (bunch charge, energy, etc.) are varied. The system we presented is, we believe, a viable candidate for the NLC design. However, a number of issues remain which demand further exploration through a combination of simulation studies and real-world research and development. We would like to elucidate these issues below.

The most significant shortcoming at present is our understanding of the transverse wakefields of tapered collimators. Recent measurements have indicated a much smaller wakefield than the analytic models predict, although the agreement between electrodynamics simulation codes and the measurements appears reasonably good [33]. A predictive analytic model is essential if the design of the collimators themselves is to be optimized, and in any event the use of numerical codes to solve for the wakefields of short bunches in long tapered collimators is probably precluded by the enormous computational resources required. In particular, it is important to understand whether the near-wall wakefields are actually as severe as the analytic models predict.

Another area of concern is the damage thresholds for both spoilers and absorbers. The simple models used in this Note for predicting the single-train and long-term fatigue thresholds are somewhat unsatisfactory. This limit can be overcome by a combination of high power-density testing of materials and improved finite-element analysis of proposed collimator designs, such as the present effort for understanding the corresponding limits for the NLC positron production target.

The present collimation amplitudes are considered marginally acceptable; in particular, the vertical near-wall maximum kick is extremely large, and this is due to the small vertical collimator aperture which is needed to protect the detector from synchrotron radiation emitted in the quadrupole. While looser collimator apertures are desired, the only means available to achieve same are to reduce L^* or increase the innermost radius of the vertex detector. In the event that further study of the wakefields shows the near-wall kick to be intolerable, it may be necessary to contemplate changes to these other paramters, either of which would have a major impact on the facility.

The studies in this Note did not consider commissioning strategies or strategies for recovering from machine protection trips or other brief interruptions. The present concept for the machine protection system (MPS) requires that the primary beam be present at full rate in order to provide advanced warning of a failure in progress which puts the accelerator at risk; if there is an interruption of even 8 msec duration (one inter-train period), it is expected that MPS would limit subsequent linac pulses to production of "pilot pulses," in which the peak power density is insufficient to damage any accelerator component, until such time as 120 Hz operation was recovered [43]. The pilot pulses are likely to have an enlarged emittance, hence increased beam losses through the collimators. This presents a bootstrapping problem which has not yet been resolved.

7 The NLC Post-Linac Collimation Task Force

The members of the NLC Post-Linac Collimation Task Force are: E. Doyle, J. Frisch, R. Helm, S. Hertzbach, L. Keller, T. Raubenheimer, P. Tenenbaum, M. Woodley.

8 Acknowledgements

The authors would like to acknowledge the assistance of K. Bane and G. Stupakov for providing analytic expressions for the wakefields of tapered collimators; and the authors of Chapter 9 of the ZDR, especially J. Irwin, D. Walz, and F. Zimmermann, without whose efforts this Note would have been impossible from the start.

References

[1] P. Raimondi *et al*, *Proceedings of the 2000 European Particle Accelerator Conference*, ed. Ch. Petit-Jean-Genaz, 18 (2000).

[2] P. Tenenbaum and T. Shintake, in *Annual Review of Nuclear and Particle Science*, ed. C. Quigg, V. Luth, P. Paul, v.49, 155–156 (1999).

[3] The NLC Design Group, *Zeroth-Order Design Report for the Next Linear Collider*, 555-642 (1996).

[4] http://www-project.slac.stanford.edu/lc/local/AccelPhysics/Parameters/ip_parameters.htm.

[5] http://www-project.slac.stanford.edu/lc/local/AccelPhysics/Parameters/budgets.htm.

[6] P. Raimondi and A. Seryi, "A Novel Final Focus Design for Future Linear Colliders," LCC-Note 0039 (2000).

[7] R. Brinkmann, "Estimate of Beam Halo for TESLA," talk given at *Beam Delivery and Interaction Region Workshop 2000,*
http://accelerator.dl.ac.uk/ap/bdir2000/proceedings/brinkmann.pdf.

[8] H. Burkhardt and R. Kleiss, "Beam Lifetime in LEP," in *Proceedings of the 1994 European Particle Accelerator Conference,* 1353 (1994).

[9] I. Reichel, *Study of Transverse Beam Tails at LEP,* CERN-Thesis-98-017 (1998).

[10] I. Reichel, F. Zimmermann, T.O. Raubenheimer, P. Tenenbaum, "Thermal-Photon and Residual-Gas Scattering in the NLC Beam Delivery," SLAC-PUB-8012 (1998).

[11] P. Tenenbaum, "Beam-Gas and Thermal-Photon Scattering in the NLC Main Linac as a Source of Beam Halo," LCC-Note-0051 (2000).

[12] N. Phinney, private communication.

[13] N.J. Walker *et al*, "Third-Order Corrections to the SLC Final Focus," in *Proceedings of the 1993 Particle Accelerator Conference* (1993).

[14] Stanford Linear Accelerator Center, oral tradition/common knowledge.

[15] T.O. Raubenheimer, P. Emma, S. Kheifets, "Chicane and Wiggler-Based Bunch Compressors for Future Linear Colliders," in *Proceedings of the 1993 Particle Accelerator Conference,* 635 (1993).

[16] R.H. Helm *et al*, "Evaluation of Synchrotron Radiation Integrals," in *Proceedings of the 1973 Particle Accelerator Conference,* 900 (1973).

[17] D. Burke, private communication.

[18] M.C. Ross *et al*, "Single Pulse Damage in Copper," in *Proceedings of the 20th International Linac Conference,* (2000).

[19] P. Lof, ed., *Elsevier's Periodic Table of the Elements* (1987).

[20] E.A. Brandes and G.B. Brook, eds., *Smithells Metals Reference Book, Seventh Edition* (1992).

[21] G.S. Brady, H.R. Clauser, J.A. Vaccari, eds., *Materials Handbook, Fourteenth Edition* (1997).

[22] J. Frisch, private communication.

[23] D.P. Pritzkau, R.H. Siemann, "Results of an RF Pulsed Heating Experiment at SLAC," in *Proceedings of the 20th International Linac Conference* (2000).

[24] X.E. Lin and D. H. Whittum, "Image Current Heating on Metal Surface Due to Charged Bunches," SLAC-PUB-8393 (2000).

[25] *ZDR*, 575.

[26] *Particle Data Book*, 1998 edition, page 148.

[27] *Particle Data Book*, 2000 online edition, section 23.4.3.

[28] K. Yokoya, "Impedance of Slowly Tapered Structures," CERN-SL-90-88-AP (1990).

[29] G. Stupakov, "Geometrical Wake of a Smooth Flat Collimator," SLAC-PUB-7167 (1996).

[30] K. Bane, private communication.

[31] K.L.F. Bane, C.K. Ng, and A.W. Chao, "Estimate of the Impedance Due to Wall Surface Roughness," in *Proceedings of the 1997 Particle Accelerator Conference* (1997).

[32] *ZDR*, 617 (1996).

[33] P. Tenenbaum *et al*, "Direct Measurements of Geometric Wakefields from Tapered Rectangular Collimators," in *Proceedings of the 20th International Linac Conference* (2000).

[34] A. Piwinski, "Wake Fields and Ohmic Losses in Flat Vacuum Chambers," DESY HERA 92-04 (1992).

[35] *ZDR*, 595-597.

[36] A. Chao, private communication.

[37] *ZDR*, 595.

[38] A. Chao, *Physics of Collective Beam Instabilities in High Energy Accelerators,* 55 (1993).

[39] R. Erickson, private communication.

[40] I. Reichel, F. Zimmermann, T.O. Raubenheimer, P. Tenenbaum, "Thermal Photon and Residual Gas Scattering in the NLC Beam Delivery", in *Proceedings of the International Computational Accelerator Physics Conference* (1998).

[41] http://www.slac.stanford.edu/xorg/ilc-trc/ilc-trchome.html.

[42] H. H. Braun *et al*, "The CLIC RF Power Source, A Novel Scheme of Two Beam Acceleration for $e^{\pm}$ Linear Colliders," CLIC Note 364 (1998).

[43] C. Adolphsen *et al*, "The Next Linear Collider Machine Protection System," in *Proceedings of the 1999 Particle Accelerator Conference,* 253 (1999).

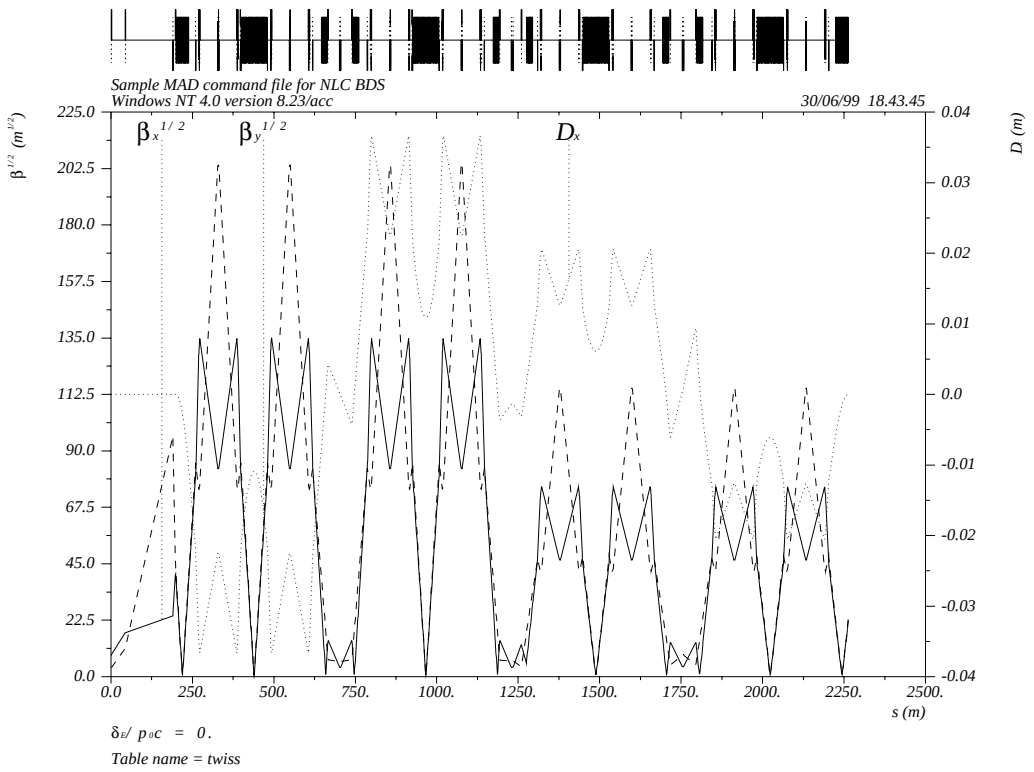

Figure 1: Twiss functions of the ZDR collimator lattice.

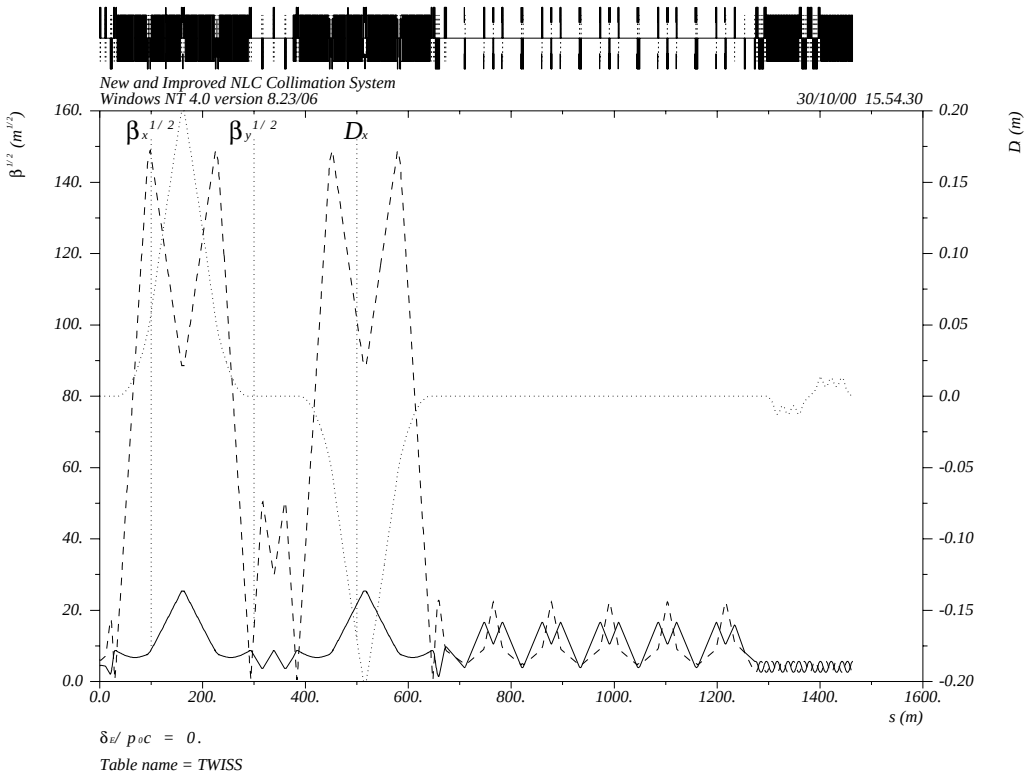

Figure 2: Optical functions of the new NLC post-linac collimation system latttice.

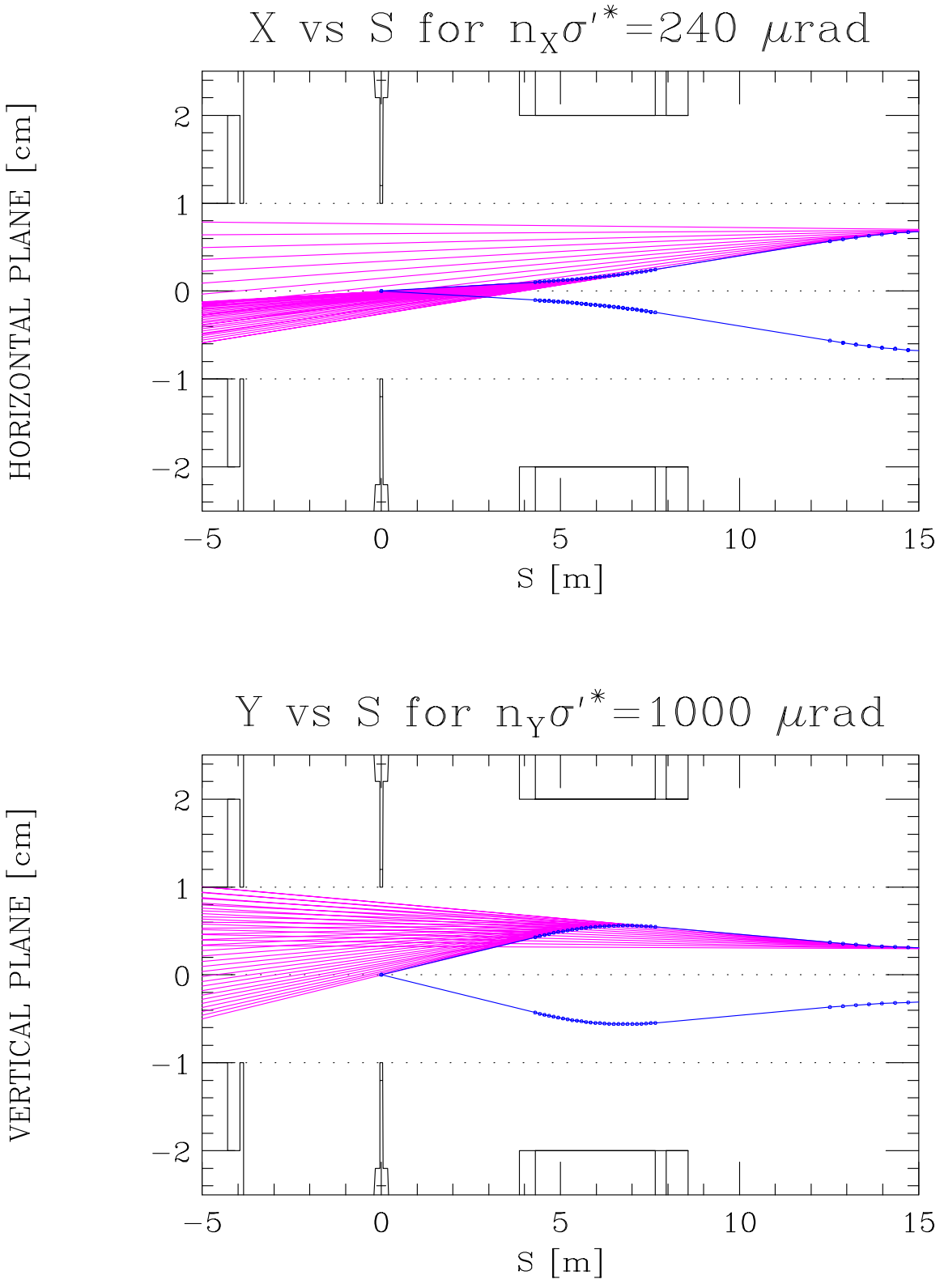

Figure 3: Synchrotron Radiation fans emitted by particles with large amplitudes in the final doublet magnets.

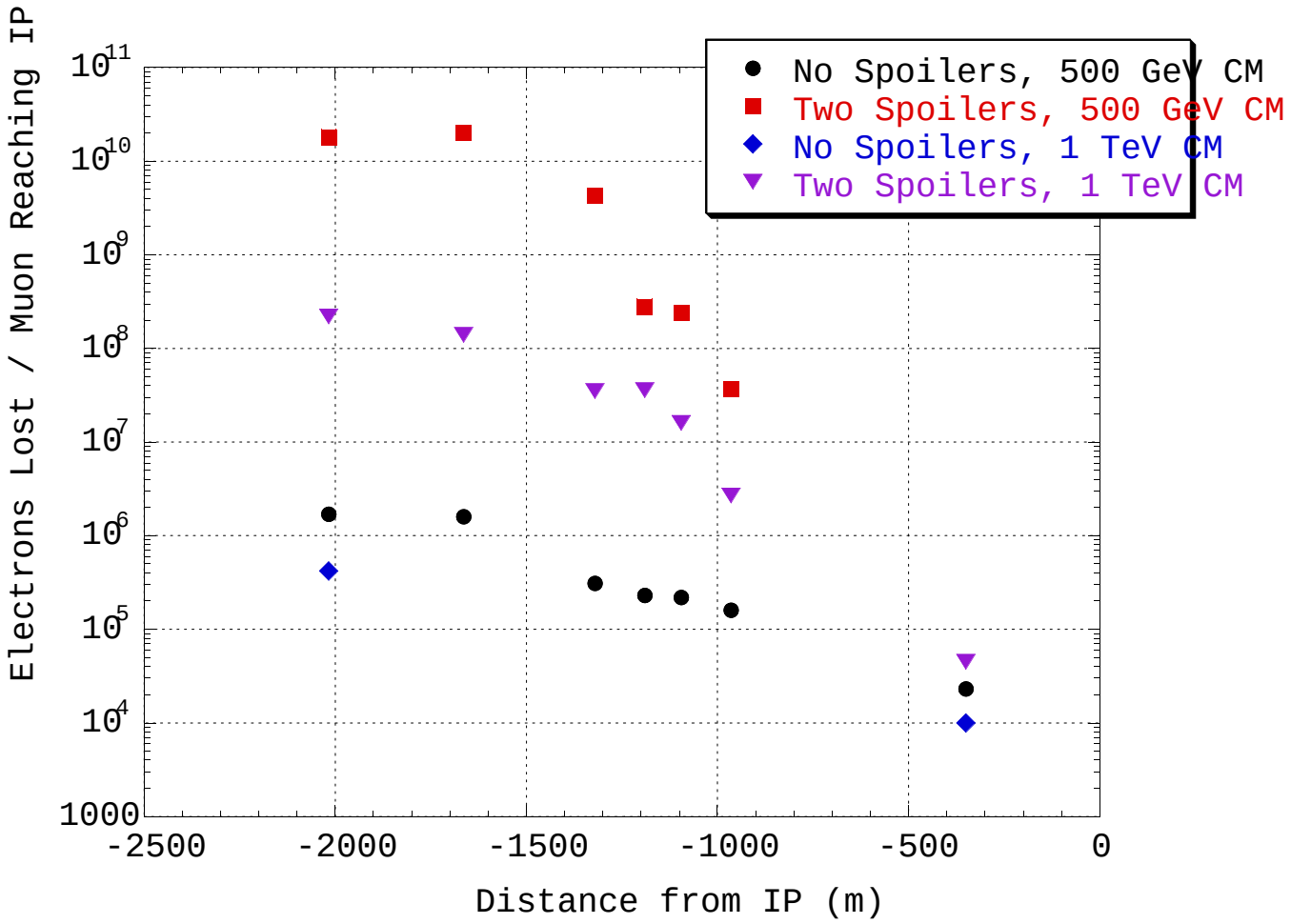

Figure 4: Plot of the muon production figure of merit as a function of distance from the IP. The figure of merit is the number of electrons which must be stopped at a given z location in order to produce a single muon in the detector. This figure is based on the 4.3 m L^* NLC FF design and the "LCD Large" detector.

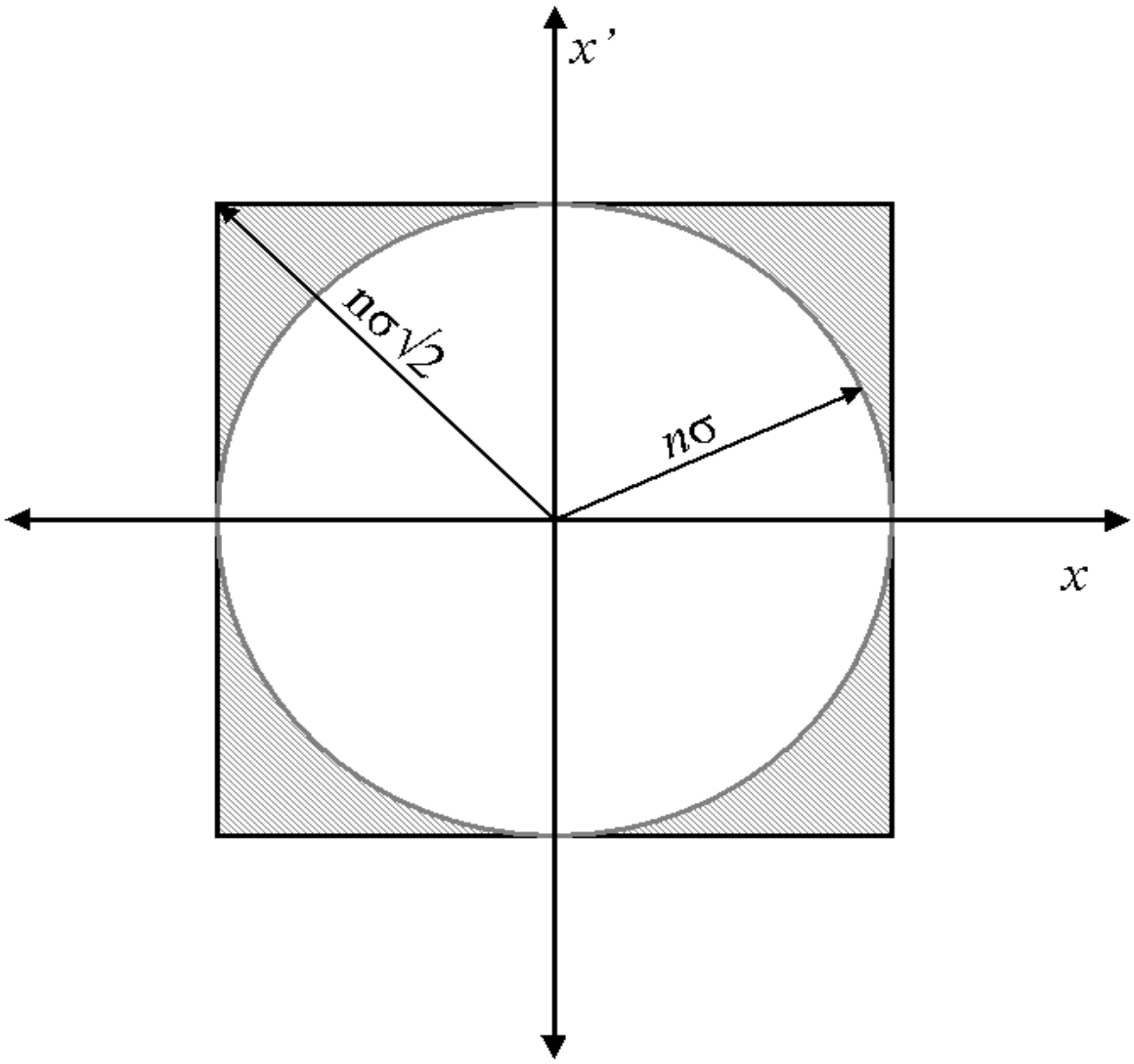

Figure 5: If collimation is performed at 90 degree intervals in betatron phase, with amplitudes of $\pm n\sigma$ in each phase, the phase space region which is transmitted is the rectangle. Note that some particles are transmitted which are outside the region of $n\sigma$ amplitude (shaded), and they may phase-rotate into the final doublet phase and generate synchrotron radiation.

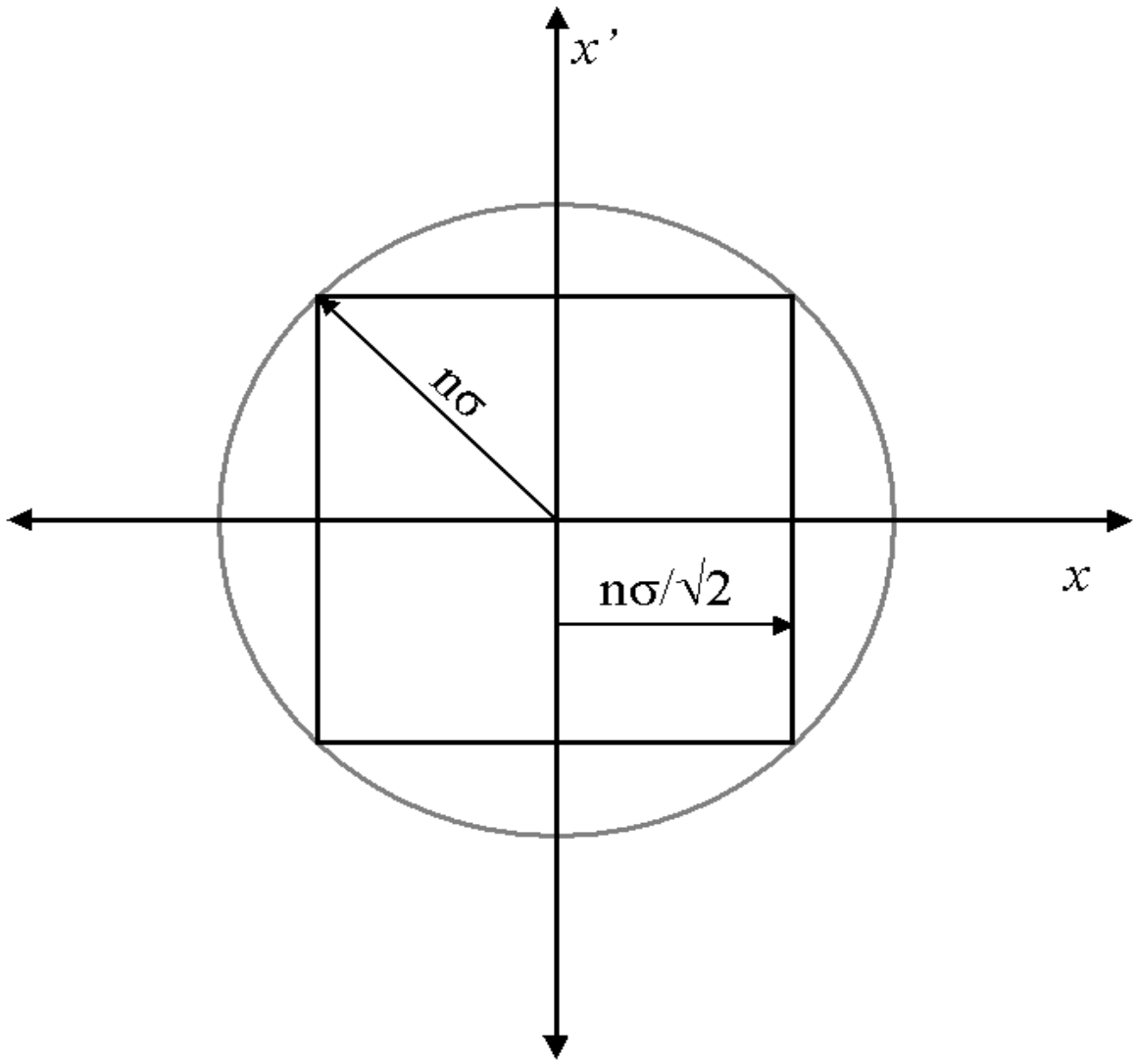

Figure 6: The phase rotation problem is resolved by collimating at $n\sigma/\sqrt{2}$, which ensures that the maximum paricle amplitude permitted is $n\sigma$.

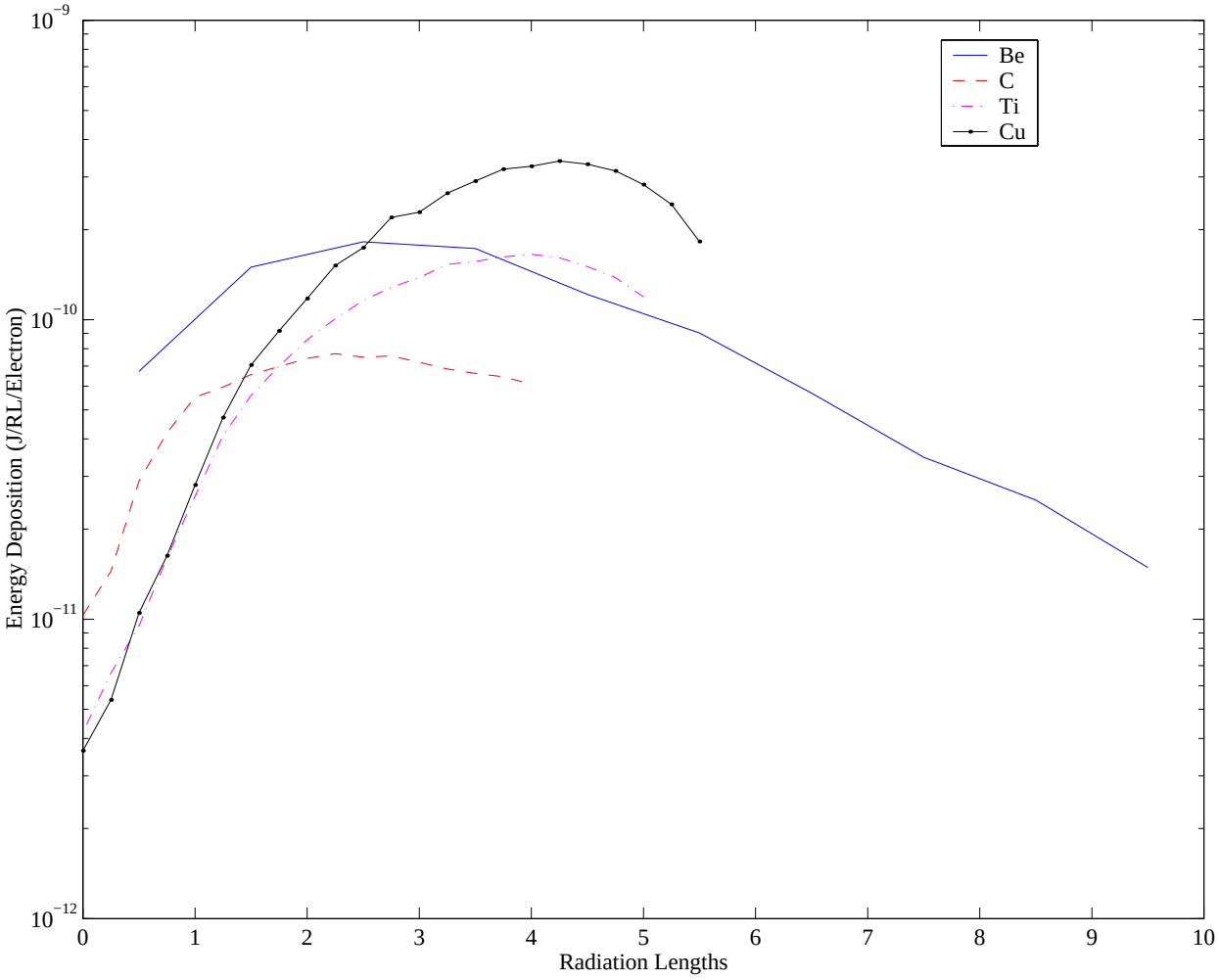

Figure 7: Energy deposition in various materials as a function of depth. Figure data courtesty J. Irwin, W.R. Nelson.

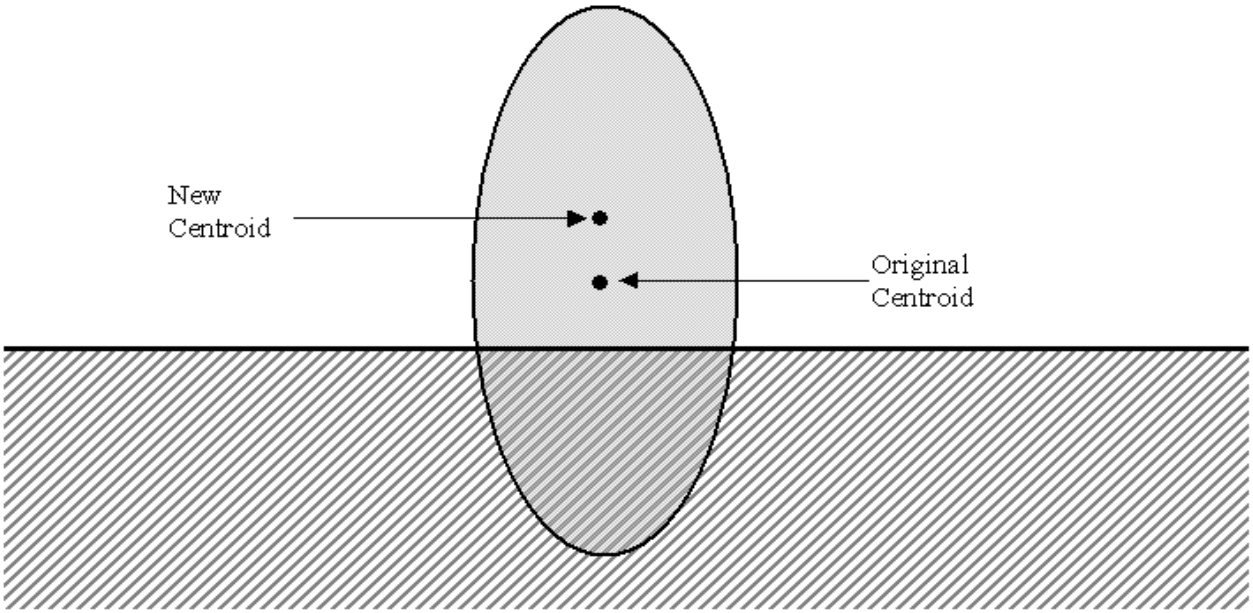

Figure 8: Schematic of a beam ellipse which is within 1 σ of the collimator jaw. If the charge which penetrates the collimator body is excluded from generation of the wakefield, the effective centroid is shifted away from the collimator jaw and the effective charge is reduced.

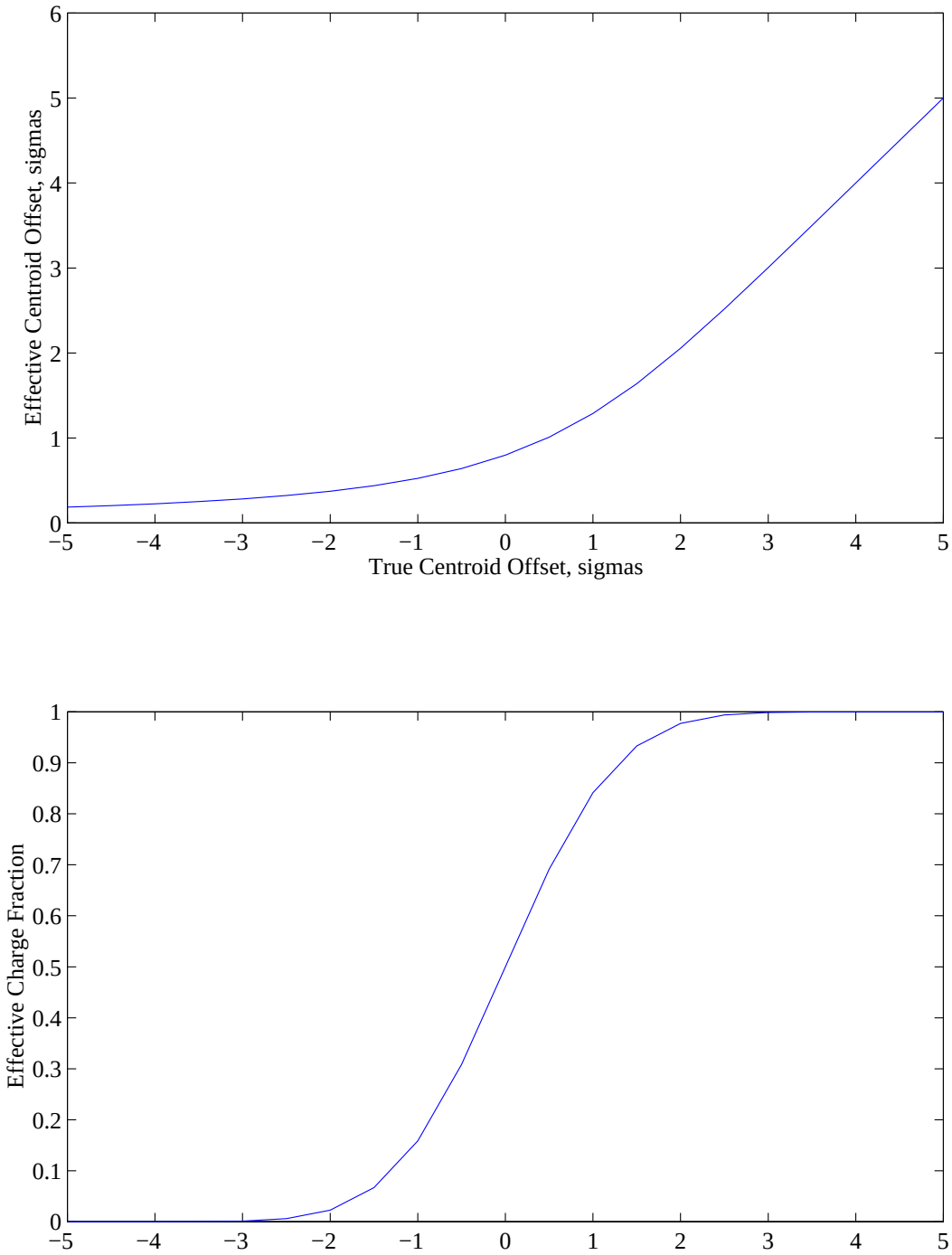

Figure 9: Change in effective centroid position and charge as a function of true centroid position for a beam near a collimator wall, assuming that particles which pass through the collimator do not participate in generation of wakefields. For positive offsets (centroid in free space far from the collimator), the difference between effective and true position and charge are both small. As the beam moves so close that the true centroid passes through the jaw the effective charge falls off quickly and the effective centroid position remains positive, as expected.

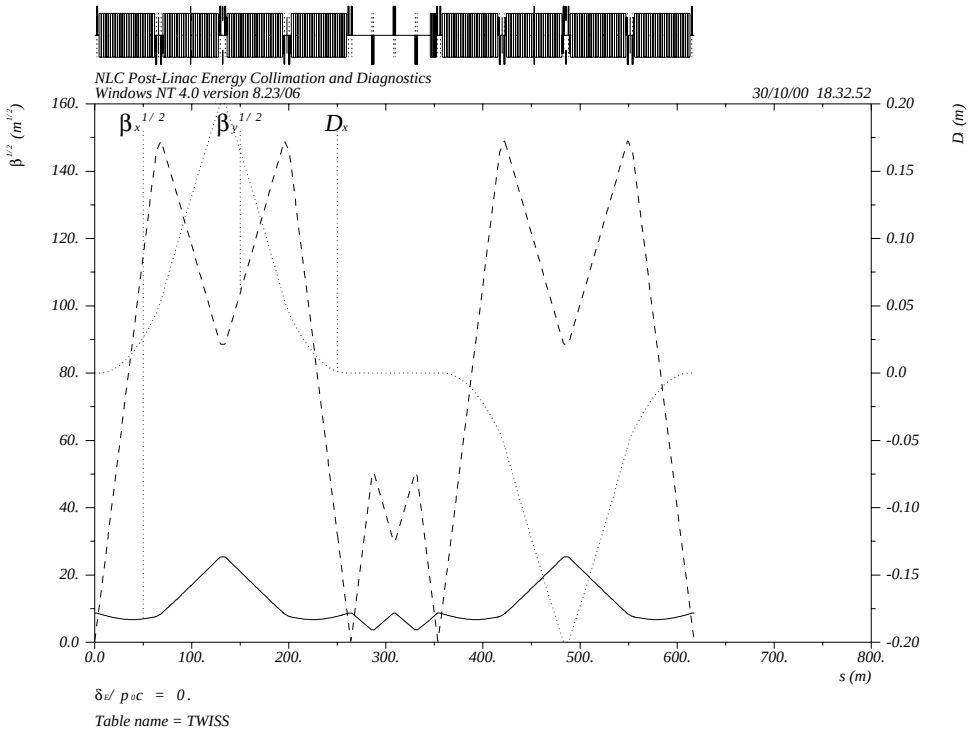

Figure 10: Optical functions for the energy collimation section.

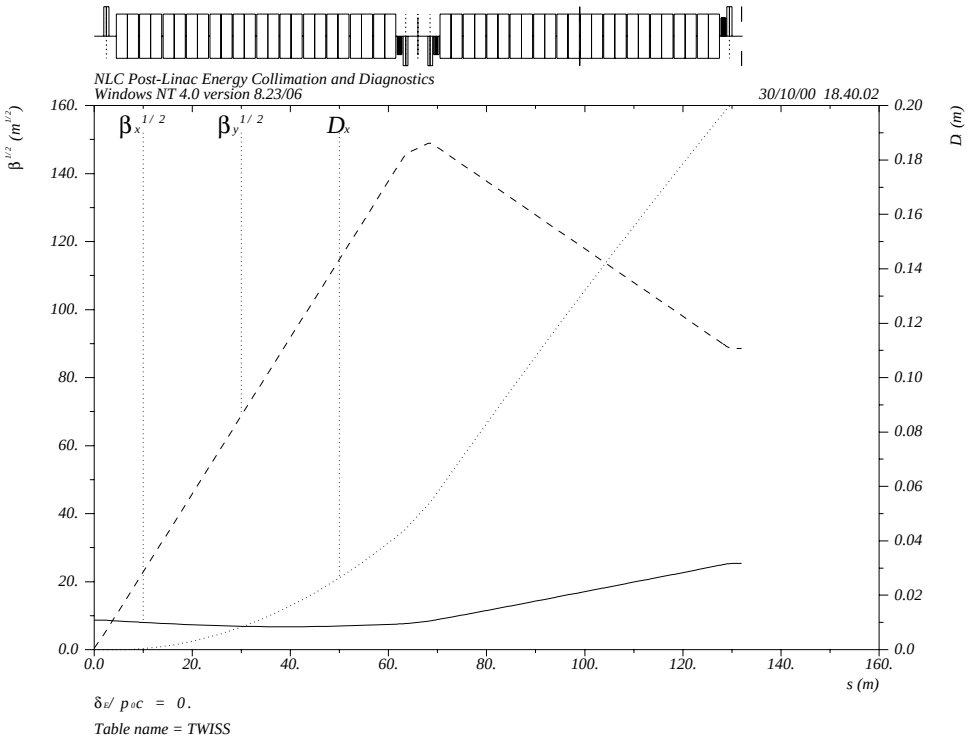

Figure 11: Optical functions for the first half of the first module of the energy collimation section. The spoiler is in the middle of the second long bend string, at $z \approx 100$ meters, and the absorber is at the end of the region shown.

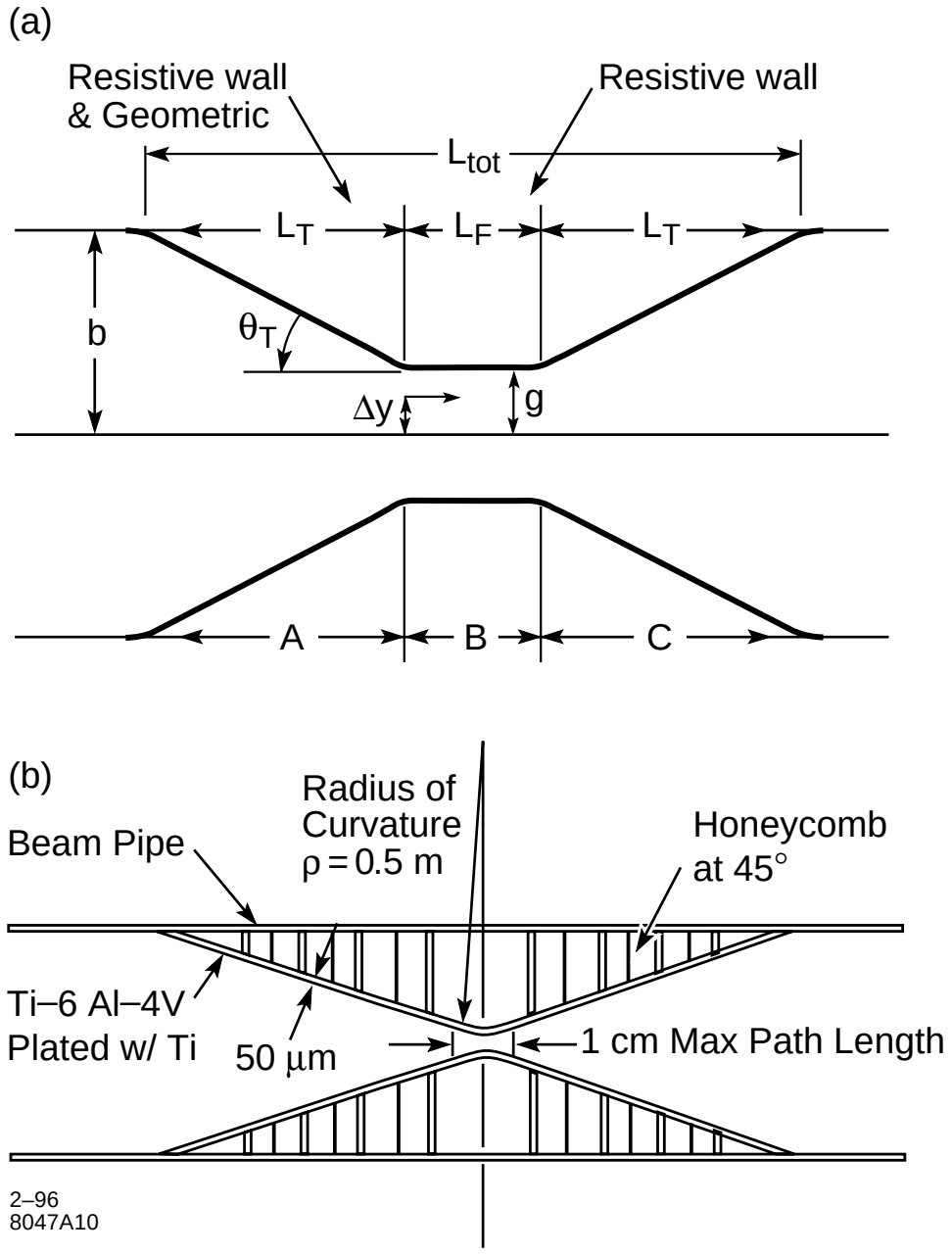

Figure 12: Tapered absorber (top) and spoiler (bottom), as proposed for energy collimation section.

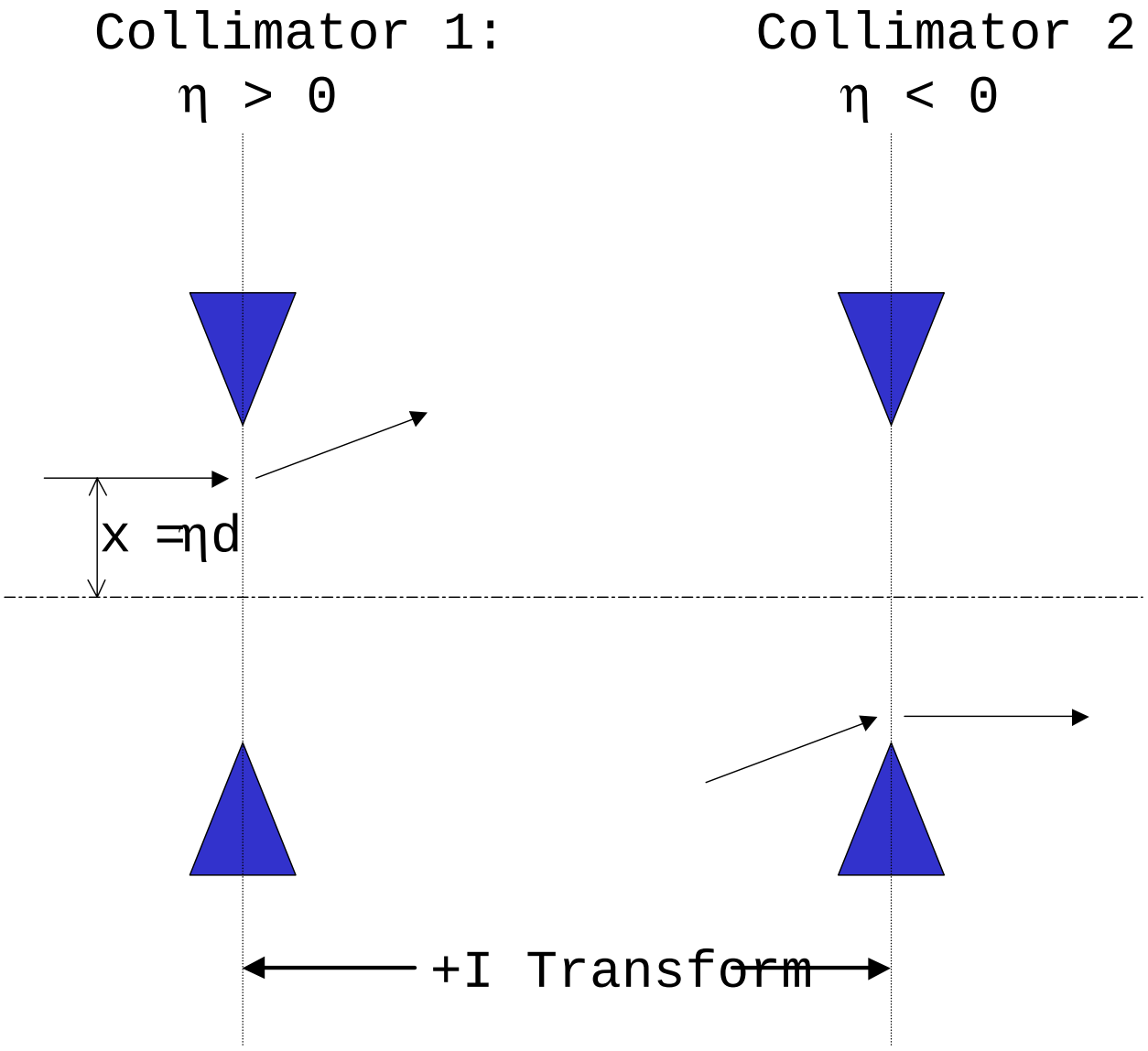

Figure 13: Principle behind cancellation of collimator wakefields in energy collimation section: for pure $\eta\delta$ offsets the first collimator produces a kick angle proportional to $\eta\delta$, which is preserved through a $+I$ transformation to a second collimator at a location where the dispersion has the opposite sign. The two kicks cancel to first order.

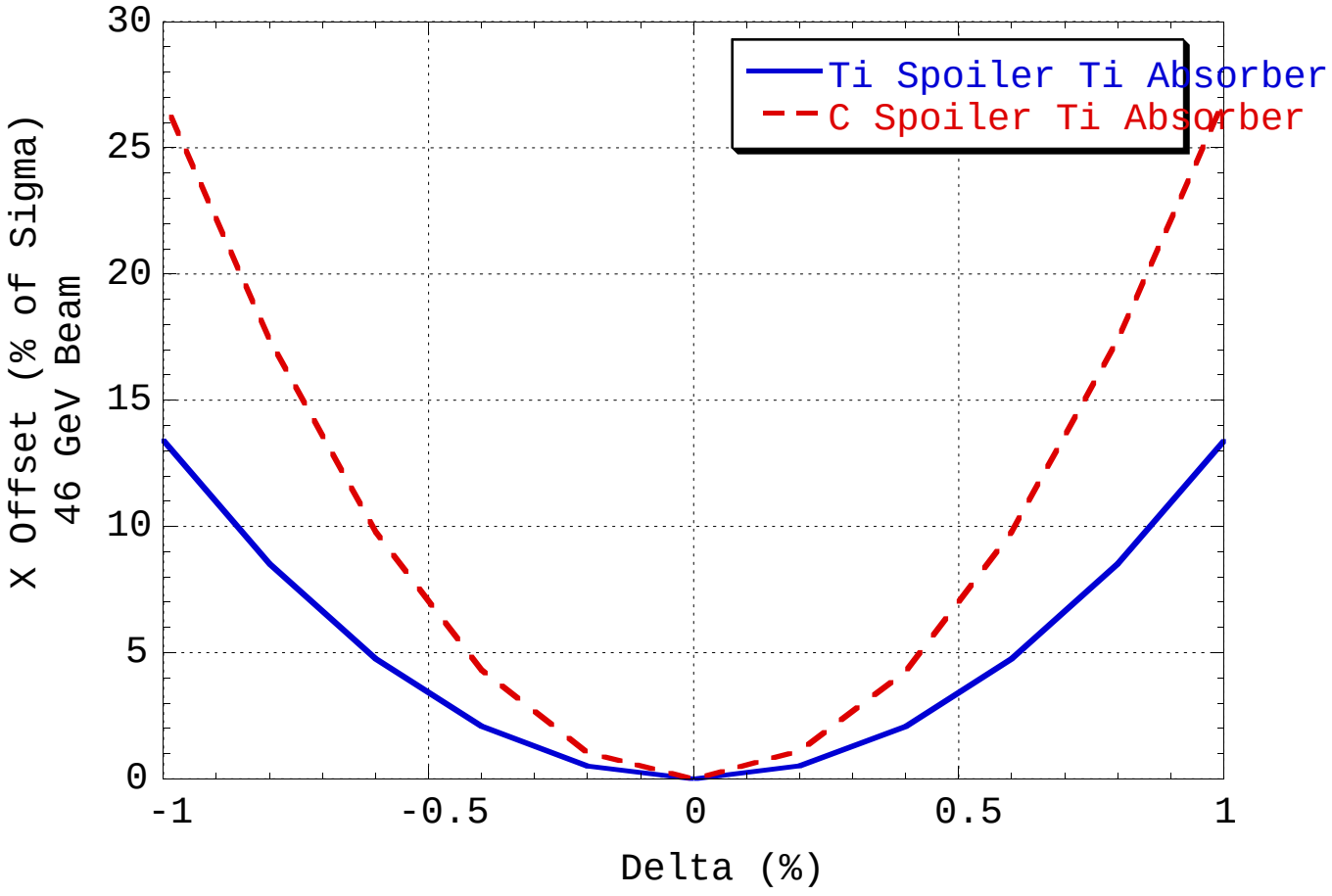

Figure 14: Effectiveness of energy collimation wakefield jitter cancellation. Resulting centroid amplitude (in beam sigmas) for a given energy centroid offset is shown for Z-peak, Case "A" parameters, which give the worst-case effect. This cancellation reduces the energy-betatron jitter coupling by about a factor of 5.

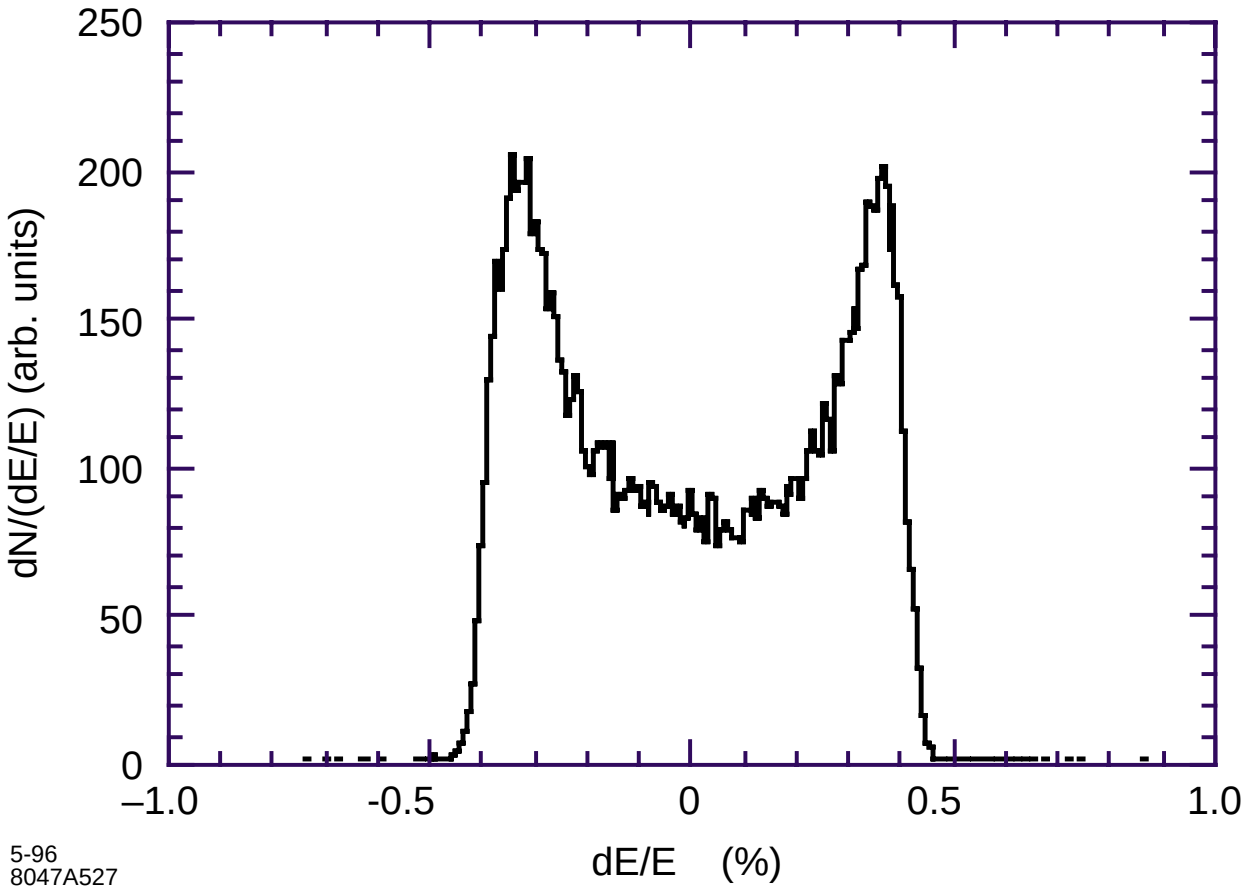

Figure 15: Energy spectrum of NLC beam in beam delivery system.

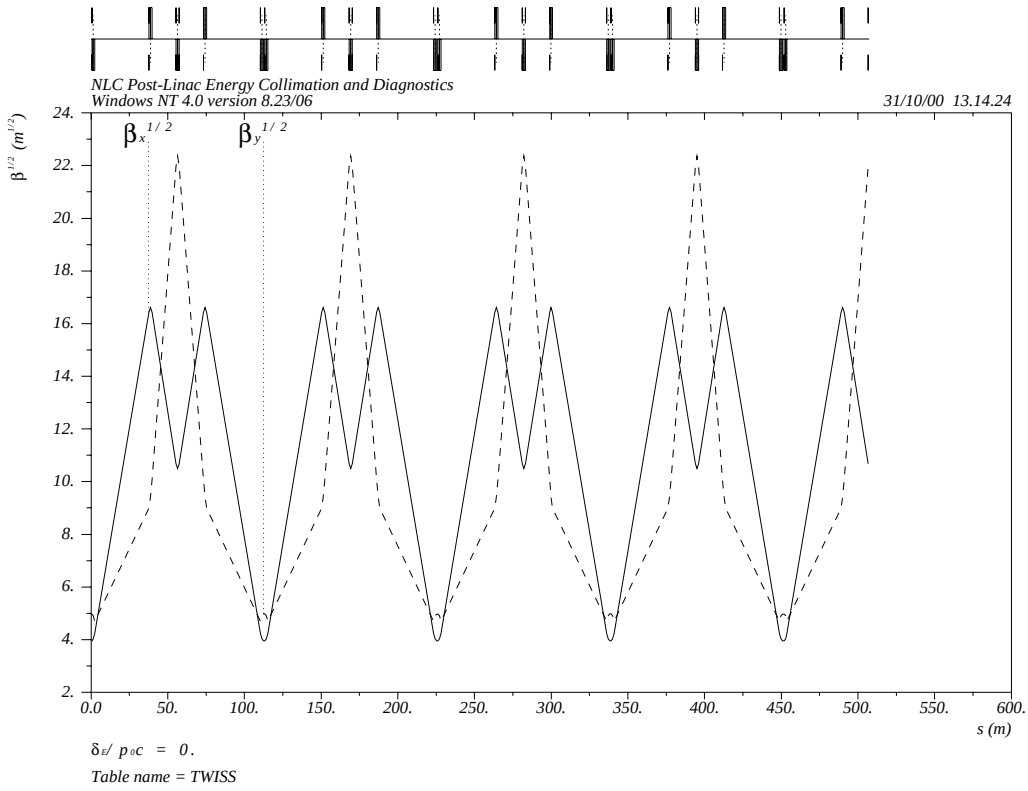

Figure 16: Twiss parameters of the betatron collimation section.

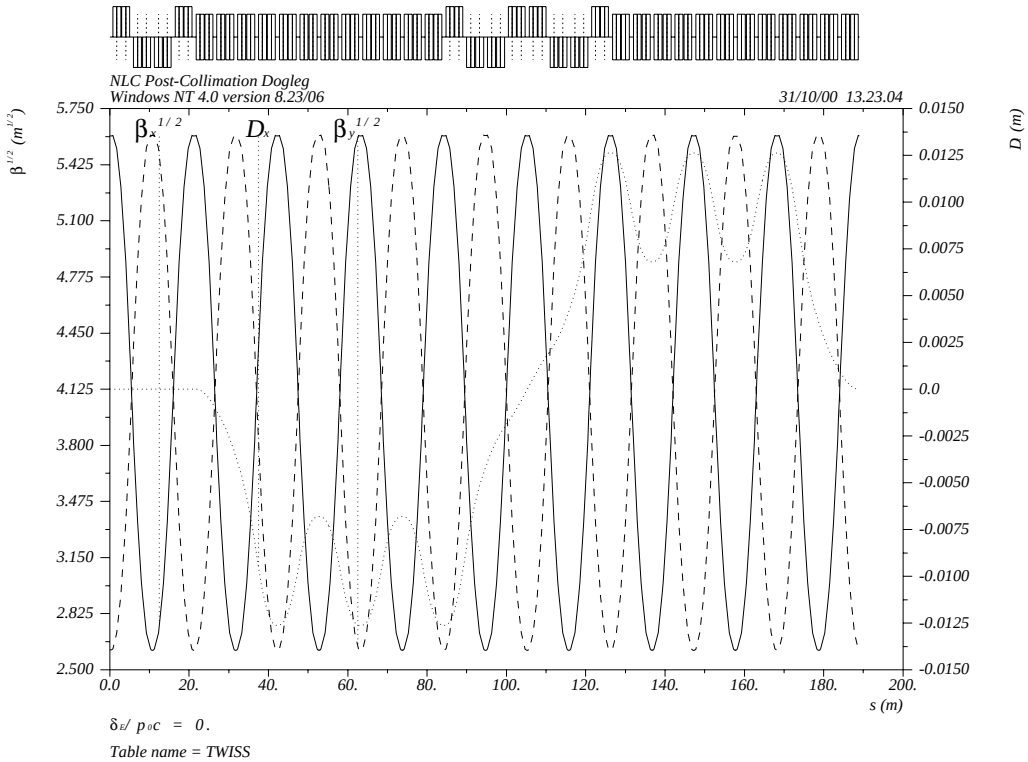

Figure 17: Optical functions of the post-collimation dogleg.

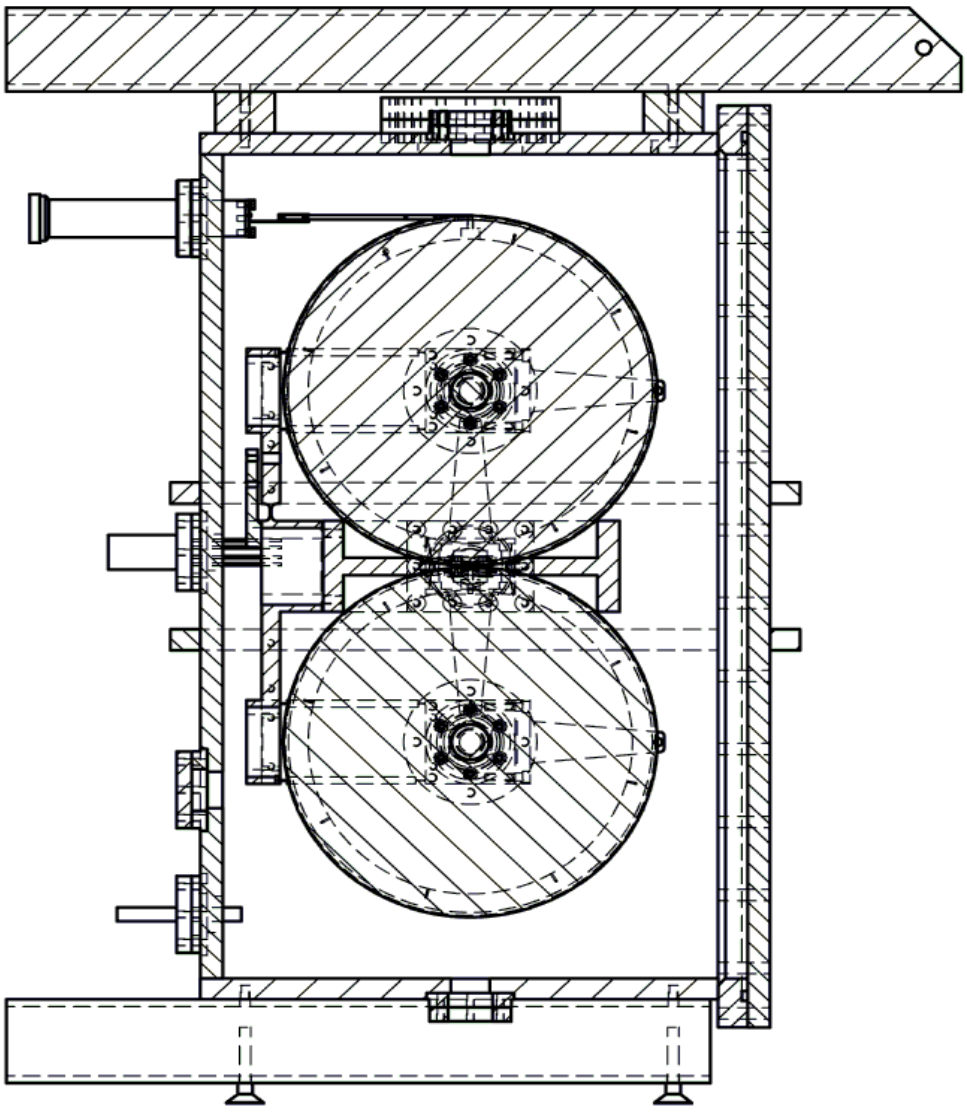

Figure 18: Consumable spoiler design, beam's-eye view. The two wheels perform the collimation and are capable of rotating when damaged to present an undamaged surface to the beam.

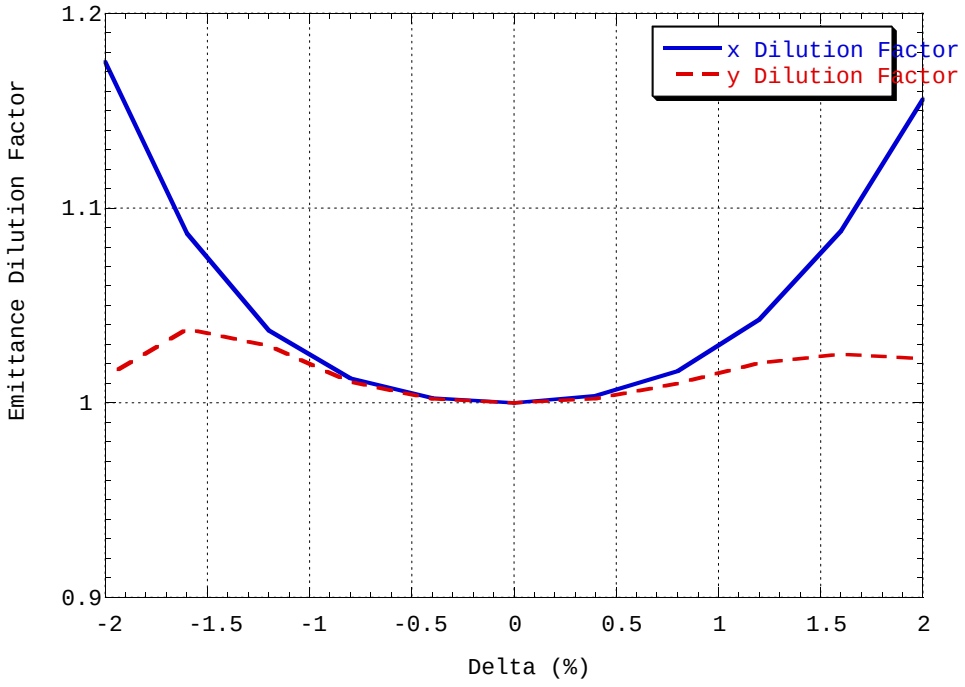

Figure 19: Emittance dilution factor for monochromatic beams with energy centroid offset. Damping ring emittances and 500 GeV beams were used.

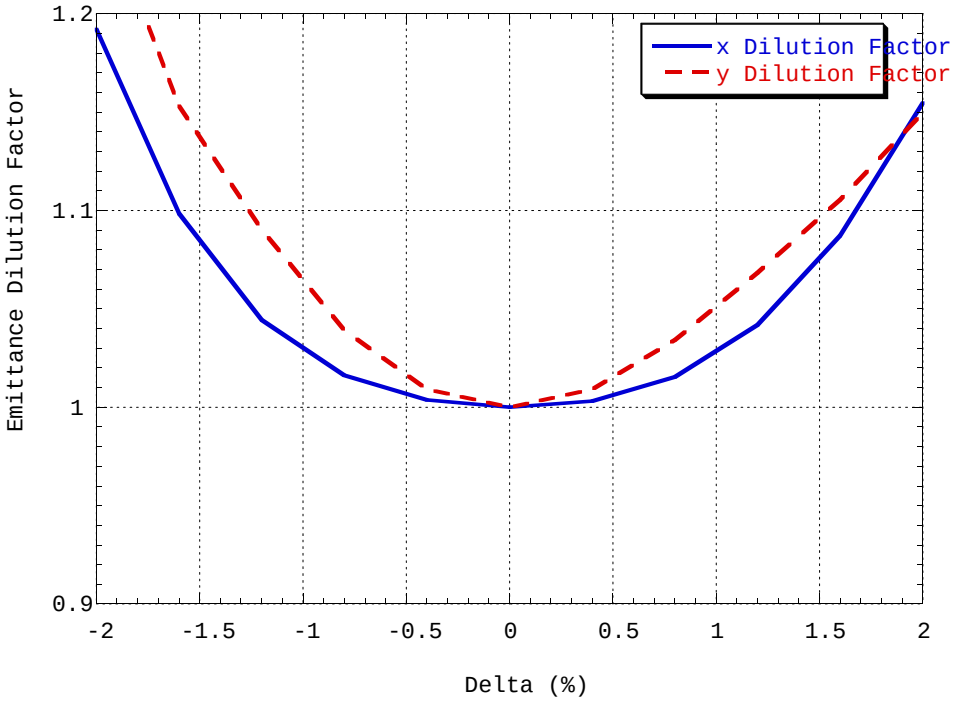

Figure 20: Emittance dilution factor for monochromatic beams with energy centroid offset. Case "C" emittances and 45.6 GeV beams were used. The reduced vertical bandwidth indicates the presence of chromogeometric aberrations.

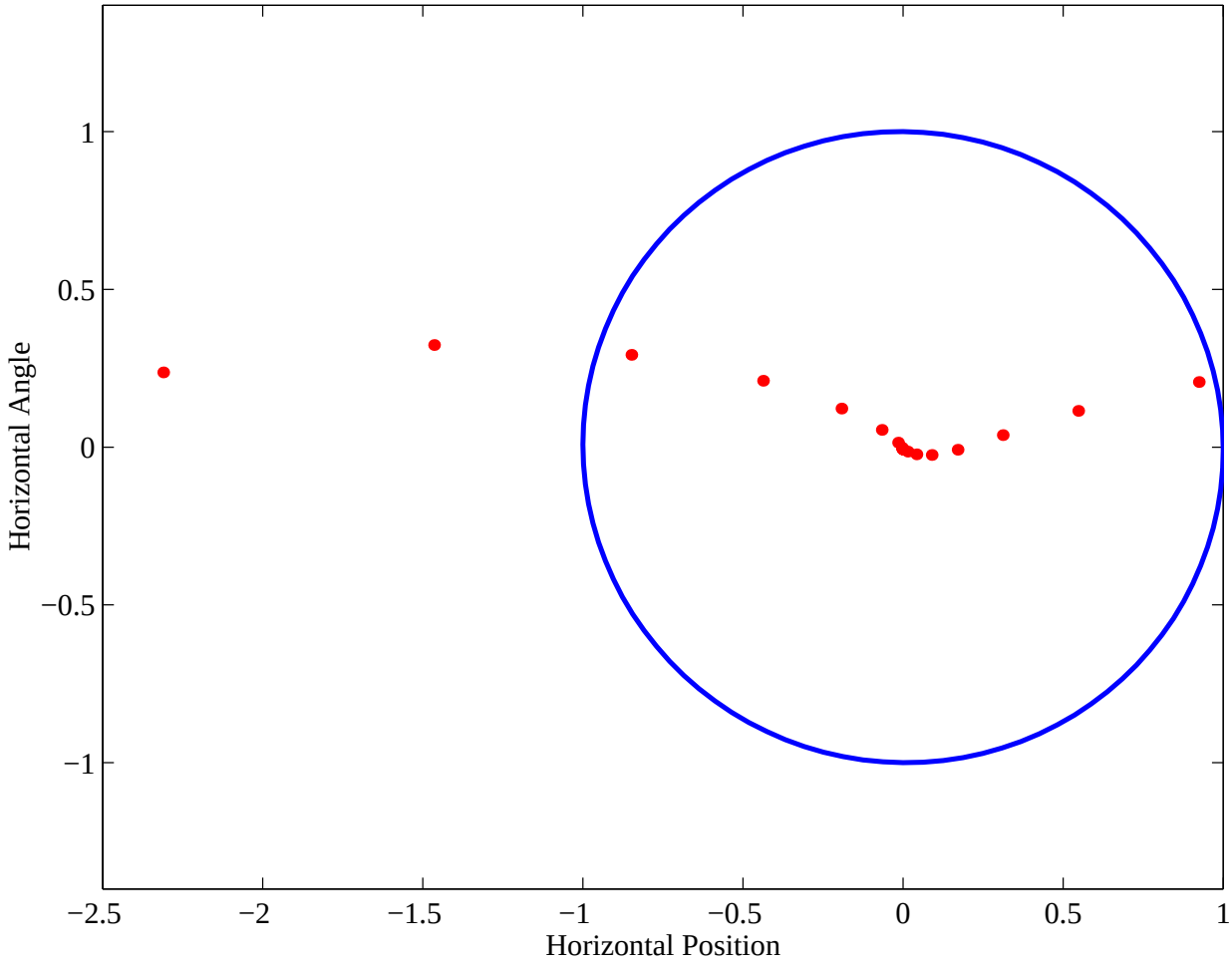

Figure 21: Centroids of monochromatic beams with energy offsets (red dots) compared to the 1 σ design phase space in (x, x') for minimum geometric emittances.

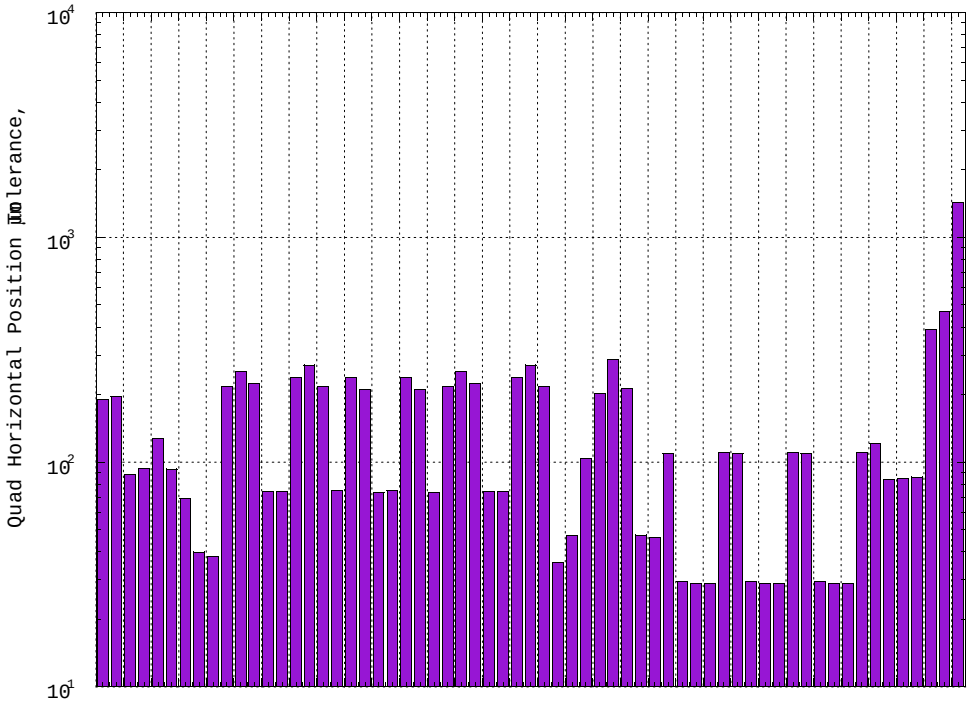

Figure 22: Maximum allowed quadrupole horizontal motion based on preventing primary beam from hitting the collimators.

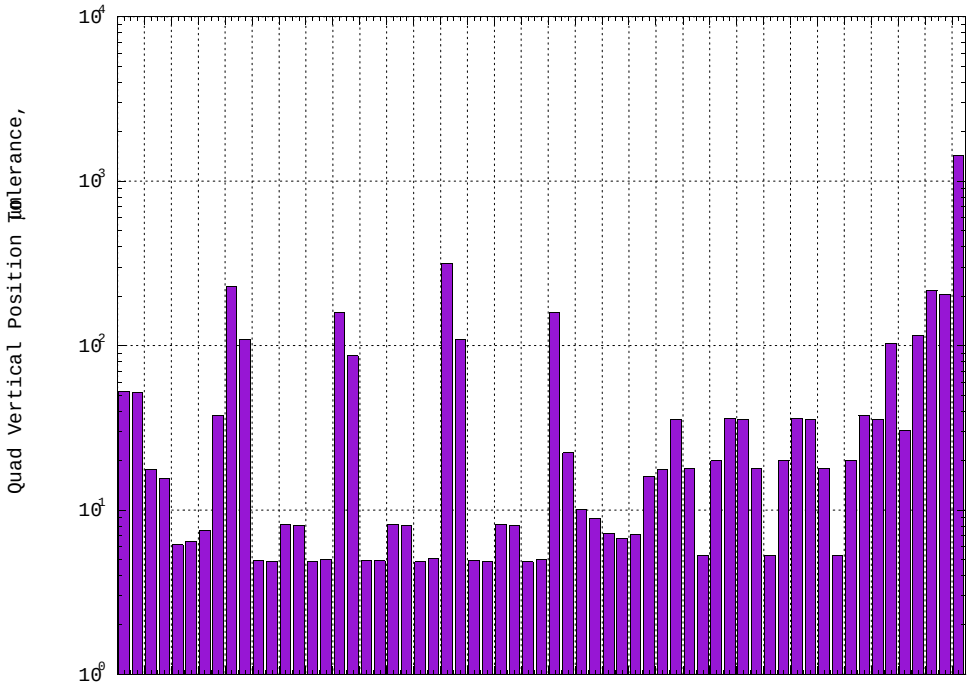

Figure 23: Maximum allowed quadrupole vertical motion based on preventing primary beam from hitting the collimators.

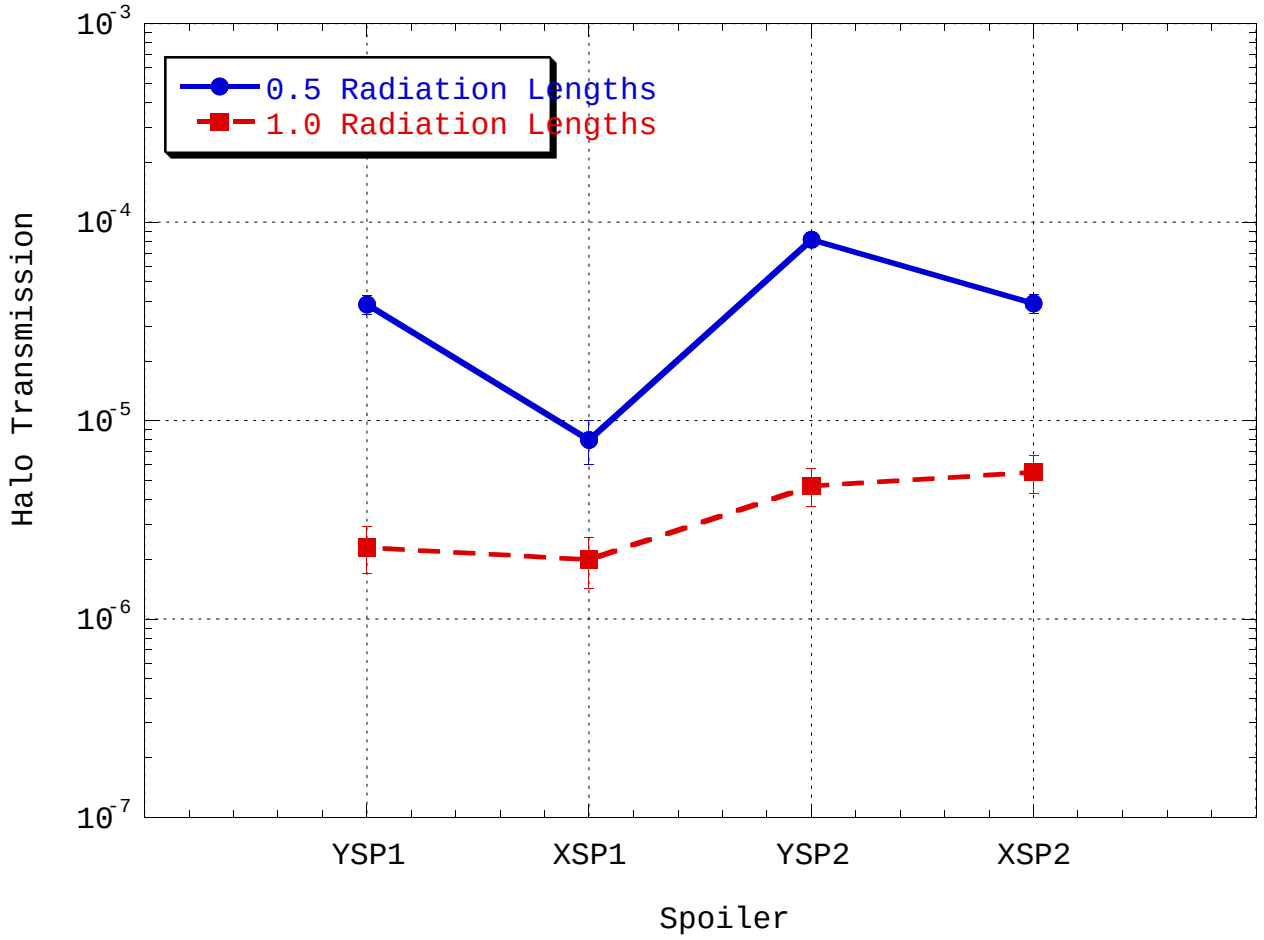

Figure 24: Halo transmission for 500 GeV particles which are incident upon the first 4 spoilers of the betatron collimation system, near the spoiler edge.